Gas flaring activity and black carbon emissions in 2017 derived from Sentinel-3A SLSTR

Alexandre Caseiro[1], Berit Gehrke[1], Gernot Rücker[2], David Leimbach[2], and Johannes W. Kaiser[1,3]

[1]Max Planck Institute for Chemistry, Mainz, Germany
[2]Zebris GbR, Munich, Germany
[3]Deutscher Wetterdienst, Offenbach, Germany

Correspondence: Alexandre Caseiro (alexandre.caseiro@mpic.de)

Abstract. Gas flares are a regionally and globally significant source of atmospheric pollutants. They can be detected by satellite remote sensing. We calculate the global flared gas volume and black carbon emissions in 2017 by (1) applying a previously developed hot spot detection and characterisation algorithm to all observations of the Sea and Land Surface Temperature Radiometer (SLSTR) instrument on-board the Copernicus satellite Sentinel-3A in 2017 and (2) applying newly developed filters for identifying gas flares and corrections for calculating flared gas volumes (Billion Cubic Meters, BCM) and black carbon emission estimates. The filter to discriminate gas flares from other hot spots combines the unique flaring characteristics in terms of persistence and temperature. The comparison of our results with those of the Visible Infrared Imaging Radiometer Suite (VIIRS) nightfire data set indicates a good fit between the two methods. The calculation of black carbon emissions using our gas flaring data set and published emission factors show good agreement with recently published black carbon inventories. The data presented here can therefore be used e.g. in atmospheric dispersion simulations. The advantage of using our algorithm with Sentinel-3A data lies in the previously demonstrated ability to detect and quantify small flares and the foreseen long term data availability from the Copernicus program. Our data (GFlaringS3, flaring activity and the related black carbon emissions) are available on the Emissions of atmospheric Compounds and Compilation of Ancillary Data (ECCAD) web site (https://eccad3.sedoo.fr/#GFlaringS3, DOI 10.25326/19 (Caseiro and Kaiser, 2019)) for use in, e.g., atmospheric composition modelling studies.

1 Introduction

Industrial gas flaring (GF) occurs when flammable gas is disposed of by burning, most commonly done at the tip of a stack. This can either take place as a measure for pressure relief, or to dispose of unwanted gas. In the upstream oil and gas (UOG) industry in particular, GF occurs when the associated gas can't be sold easily and is not used on-site for energy generation.

Especially in insufficiently developed energy markets companies seem to be spared from enough economic or political incentives to collect, or convert the gas. (Rahimpour and Jokar, 2012; Emeka Ojijiagwo et al., 2016) Improvements of flare gas recovery systems has been recommended for more closely monitored facilities (Zolfaghari et al., 2017; Papailias and Mavroidis, 2018).

GF negatively impacts the immediate surrounding (Akinola, 2018), for example through noise (Ismail and Umukoro, 2012; Nwoye et al., 2014), heat stress (Anomohanran, 2012; Julius, 2011) and visual pollution (Anomohanran, 2012; Ajao and Anurigwo, 2002). GF also impacts the environment on a wider scale through the emission of pollutants and greenhouse gases like carbon dioxide, carbon monoxide, black carbon, nitrogen oxides, polycyclic aromatic hydrocarbons, volatile organic com-

5   pounds and acid rain precursors (Obioh et al., 1994; Uzomah and Sangodoyin, 2000; Nwaichi and Uzazobona, 2011; Onu et al., 2014; Li et al., 2016).

It has been estimated that between 2003 and 2012 GF produced on average 304 Tg CO_2 yearly, representing 0.6 % of the global anthropogenic emission of CO_2 equivalent (Olivier et al., 2014). The recovery of flare gas can play a relevant role in improving sustainability and meeting emissions targets. (Ahmed Osama Abdulrahman et al., 2015; Gabriele Comodi et al.,

10   2016) Elvidge et al. (2018) estimated that a suppression of GF could contribute to 2% of the global nationally determined contributions (NDC) under the United Nations Framework Convention on Climate Change Paris Agreement. Some countries could meet or even surpass their NDC (Yemen, Algeria and Iraq), while others could meet between one third to almost all of their NDC (Gabon, Venezuela, Iran and Sudan).

Of particular importance is also the black carbon (BC) emission emitted by GF. BC is a known carcinogen (Heinrich et al.,

15   1994) as well as a short-lived climate forcer (IPCC, 2013). BC strongly effects environments such as the Arctic regions through lowering the albedo of snow-covered surfaces (Flanner et al., 2007; Stohl et al., 2013; Bond et al., 2013; Huang et al., 2015; Evangeliou et al., 2018), impacting on the earth's radiative balance (Doherty et al., 2010; Quinn et al., 2007; Hansen and Nazarenko, 2004) as well as adding to the Arctic amplification phenomenon (Serreze and Barry, 2011). GF contribution to the BC global emissions was estimated to amount to 270 and 210 Gg in 2005 and 2010, respectively (Klimont et al., 2017).

20   Regionally, Stohl et al. (2013) showed that GF contributes to half the near-surface BC concentration in the Arctic.

GF is considered an important component of atmospheric dispersion simulations (Evangeliou et al., 2018) and climate modeling (Huang and Fu, 2016) as the impact of GF emissions extends beyond immediate environmental concerns. However, information on the amount of natural gas being disposed of through stack burning and the accrued emissions are sparse. Reporting is often not enforced, inconsistent or otherwise not reliable.

25   Satellite remote sensing has been utilized for regional and global identification and characterization of GF. (Casadio et al., 2012b, a; Anejionu et al., 2014; Faruolo et al., 2014; Chowdhury et al., 2014; Anejionu et al., 2015; Faruolo et al., 2018) The most prominent system is NOAA's VIIRS (National Ocean and Atmospheric Administration's Visible Infrared Imaging Radiometer Suite) Nightfire dataset (see https://ngdc.noaa.gov/eog/viirs/download_viirs_fire.html), developed by Elvidge et al. (2016) based on previous work (Elvidge et al., 2001, 2007, 2009, 2013) and leading to a globally consistent survey of GF

30   volumes available extending back to 2012.

We recently published an adaptation and extension of the VIIRS Nightfire algorithm with which observations of the Sea and Land Surface Temperature Radiometer instrument (SLSTR) on-board the Sentinel-3 satellites can be analysed, too (Caseiro et al., 2018). The algorithm detects and quantifies hot sources, including gas flares, using the night-time readings of the short-wave infrared (SWIR), mid-infrared (MIR) and thermal infrared (TIR) channels. The main advantages of using our hot spot

35   detection and characterisation algorithm lie in the ability to detect and quantify smaller flares and the foreseen long term data

availability from the series of Sentinel-3 satellites in the Copernicus program. Additionally, SLSTR observations (night-time overpasses at 10:00 PM) complement those of VIIRS (1:30 AM) by filling observation gaps in the time series.

Here, we describe a new dataset of global GF volume (Billion Cubic Meters, BCM) and BC emissions, which we have derived from all Sentinel-3 SLSTR observations in 2017. Chapter 2 describes newly developed methods for identifying gas
5 flares among the observed hot sources, correcting for intermittent observations opportunities, and dynamically determining appropriate BC emission factors from the observations. The results of applying the hot source detection and characteristion algorithm plus the newly developed methods to all SLSTR observations of 2017 are presented in Chapter 3. Finally, our conclusions are summarised in Chapter 4.

2 Methods

10 ### 2.1 Hot spot detection and characterization

An overview of the steps involved in the study presented here are outlined in Figure 1.

We base our work on the persistent hot spots detection and characterisation algorithm described in Caseiro et al. (2018) to process a full year (2017) of Sentinel-3A's Sea and Land Surface Temperature Radiometer (SLSTR) data. Using radiometrically calibrated radiance data as input, our algorithm detects hot spots and fits the sum of two Planck curves: one representing the
15 hot source and the other the cool background. Both curves are fitted to the night-time spectral infrared (short-wave, mid-wave and thermal infrared: SWIR, MIR and TIR) observations to characterize temperature and area of the observed gas flares. Additionally, we calculate the radiative power of the flare using the Stefan-Boltzmann equation.

While in principle the methodology used is based on the Nightfire algorithm developed for Visible Infrared Imaging Radiometer Suite (VIIRS) (Elvidge et al., 2013, 2016), it differs by (1) analysing the radiances of clusters of contiguous hot pixels
20 instead of treating spatial maxima as individual pixels and (2) using the TIR channels when fitting the sum of the two Planck curves. We expect the resulting gas flare representation to be more realistic and accurate for the characterisation of large gas flare arrays as well as for smaller flares and a more stringent constraining of the background temperature.

We already tested the method using oil and/or gas producing regions within a limited timespan and compared the results to the VIIRS Nightfire "flares only" product (Caseiro et al., 2018). The results showed a good agreement of our hot source
25 detection when investigating persistent hot spots with the advantage of the Sentinel-3A's SLSTR algorithm in detecting and quantifying smaller flares, due to the night-time availability of a second SWIR channel. The characterisation (temperature, area and radiative power) also reached similarity although temperatures were slightly lower, whereas areas and radiative power were slightly larger in our results.
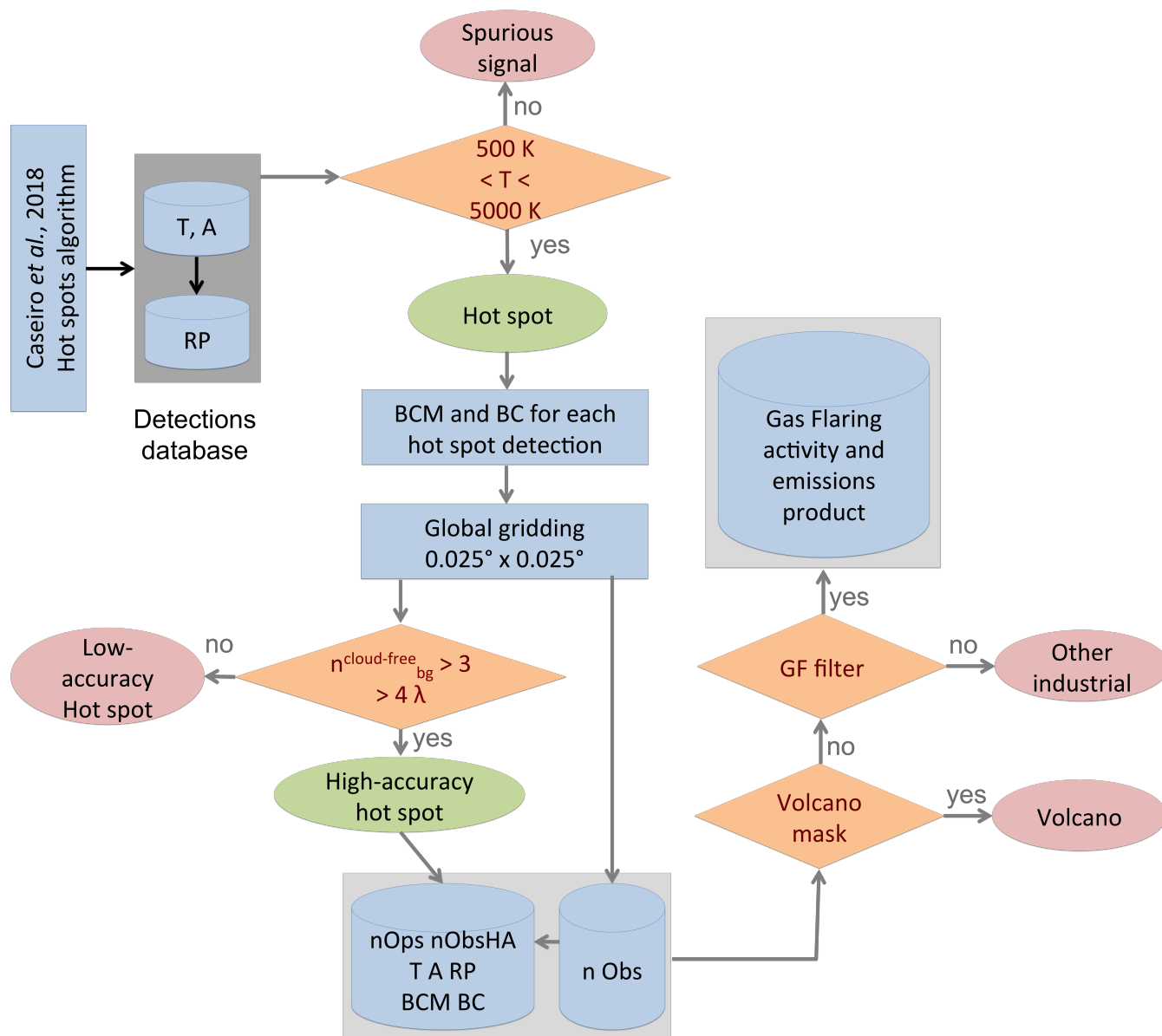
Figure 1. Flowchart of the methodology used in the present work. Starting point is the hot spot algorithm detection decribed in Caseiro et al. (2018) which, after applying a filter on the retrieved temperature (500 K < T < 5000 K), produces a database of hot spots detections. For each of these hot spot detections, the activity (Billion Cubic Meters, BCM) and Black Carbon (BC) emissions are computed. All hot spot detections are gridded into a global 0.025° × 0.025° grid. For each grid cell, the following quantities are computed: the number of detections, of high-accuracy detections and of days of detecion (see below, Section 2.2.2), temperature, area and radiative power (minimum, average, maximum and standard deviation), the date of the first and the last detection and the sum of the activity (BCM) and BC emissions. A volcano filter is applied to the global grid in order to mask out volcanic activity (see Section 2.2.1). The last step is the discrimination of grid cells for flaring activity (see Section 2.2.2).

2.2 Hot spot classification

2.2.1 Volcano filter

In order to filter out volcanic activity from our dataset, we use the data available from the Global Volcanic Program of the Smithsonian institution. (Venzke, 2013) The data was filtered for any eruption in 2017 and we computed a mask at the 0.025 degrees resolution. A buffering zone of $0.25°$ was used because the center coordinates specified may not correspond to the center of volcanic activity. Many volcanoes do not consist of a single edifice, but a volcanic field with many individual eruptive fissures through which lava erupts. (Siebert et al., 2010)

2.2.2 Discrimination of gas flares from other industrial hot sources

In order to discriminate gas flares from other night-time hot spots we investigate persistence and retrieval temperature filtering. We project all the hot spot detections onto a 0.025×0.025 degrees global grid. This is a spatial resolution which reflects the reality on the ground, where several flares, separated by tens to hundreds of meters, may be operated within a single oil and gas facility, while facilities are tens of kilometers apart. The following quantities are then computed for each grid cell: the number of hot spot detections (n_{Obs}), the number of high-accuracy (Caseiro et al., 2018) hot spot detections (n_{ObsHA}), the minimum, maximum, average and standard deviation of the high-accuracy hot spot retrieved temperature (T), area (A) and radiative power (RP) as well as the earliest and the latest hot spot observation date.

The temperature filtering we test is based on Elvidge et al. (2016) and on the recent work by Liu et al. (2018), who derived gas flaring temperatures of 1000 K to 2600 K from the VIIRS Nightfire database, depending on the type of operation (shale oil or gas, offshore, onshore or refinery). Most of the gas flares display temperatures between 1650 K and 1850 K. However, temperatures can occasionally be as low as 1300 K. This overlaps with particularly hot detections from the coal chemical industry and steel plants. Therefore, additional criteria are needed for identifying gas flares in the hot source dataset.

In order to select the discriminating strategy we test several subsets of the hot spot database. For each subset described in Table 1, a sample of 100 random onshore grid cells have been tested by examining high-resolution imagery (Google Earth) and the locations are classified into four categories:

Flare (F) flaring site with visible flame

Likely (L) industrial or oil extraction site with typical flaring infrastructure but no visible flame

Unlikely (U) industrial site without typical flaring infrastructure

No industry (N) e.g. agricultural or forested area.

The subsets are characterized in terms of user's accuracy (Equation 1) and commission error (Equation 2).

$$User's\ accuracy = \left(F + \frac{L}{2} \right) \pm \frac{L}{2} \tag{1}$$

Table 1. User's accuracy (UA, %) and commission error (C, %) of the hot spot discrimination strategies considered.

$n_{Obs} >$	–	3	4	–	–	–	–	–
$n_{ObsHA} >$	2	2	2	5	5	5	7	7
$T_{min}\ (K) >$	1000	1000	–	–	–	–	–	–
$T_{max}\ (K) >$	1400	1400	800	1200	1500	1800	1200	1500
n_{cells}	6733	5872	9469	6817	6232	5485	5527	5129
UA	84±6	86±8	60±10	77±13	85±11	88±10	73±14	87±11
C	7±3	4±2	19±11	6±4	3±1	1±1	8±5	2±1

$$Commission\ error = \left(N + \frac{U}{2}\right) \pm \frac{U}{2} \qquad (2)$$

In some industrial areas, facilities that use gas flares may be close to other hot spots, such as iron smelters or steel mills. In those cases, a commission error occurs when the flare is off and our methodology samples the other hot spot. The omission error can be divided into two categories: flares that the hot spot detection and characterization algorithm failed to detect and flares that were detected as hot spots but which the discrimination strategy left out. The former will be the same for any discrimination procedure considered.

Detections located in grid cells where the yearly maximum temperature retrieval is above 1500 K and a persistency and quality criterion ($n_{ObsHA} > 5$) is met are considered as originating from gas flares and called flaring locations hereafter. This achieves a relatively large number of grid cells with detections, i.e. low omission error, combined with a high user's accuracy and a low commission error of 85±11% and 3±1%, respectively. Inserting a limitation on the minimum temperature or increasing the maximum temperature or the number of high-accuracy observations would not significantly increase the user's accuracy or decrease the commission error, but would reduce the number of grid cells complying to the discrimination criteria by several hundreds, which we interpret as an increase in the omission error.

2.3 Determination of flared volumes and black carbon emissions

In order to compute the activity and emissions, we estimated the number of days of operations per site by expressing the maximum number of observations as a function of latitude (in 10° bins, see Figure 2). The function computes the maximum number of observations ($nObs_{max}$) per grid cell for a given latitude which we assume expresses a continuous hot spot (365 days a year). The number of days of operation is then estimated by scaling following Equation 3. By this scaling, we take into consideration the limitations of gas flaring detection from space (cloud cover and overpass frequency).

$$n_{Ops} = n_{Obs} \times \frac{365}{nObs_{max}} \qquad (3)$$
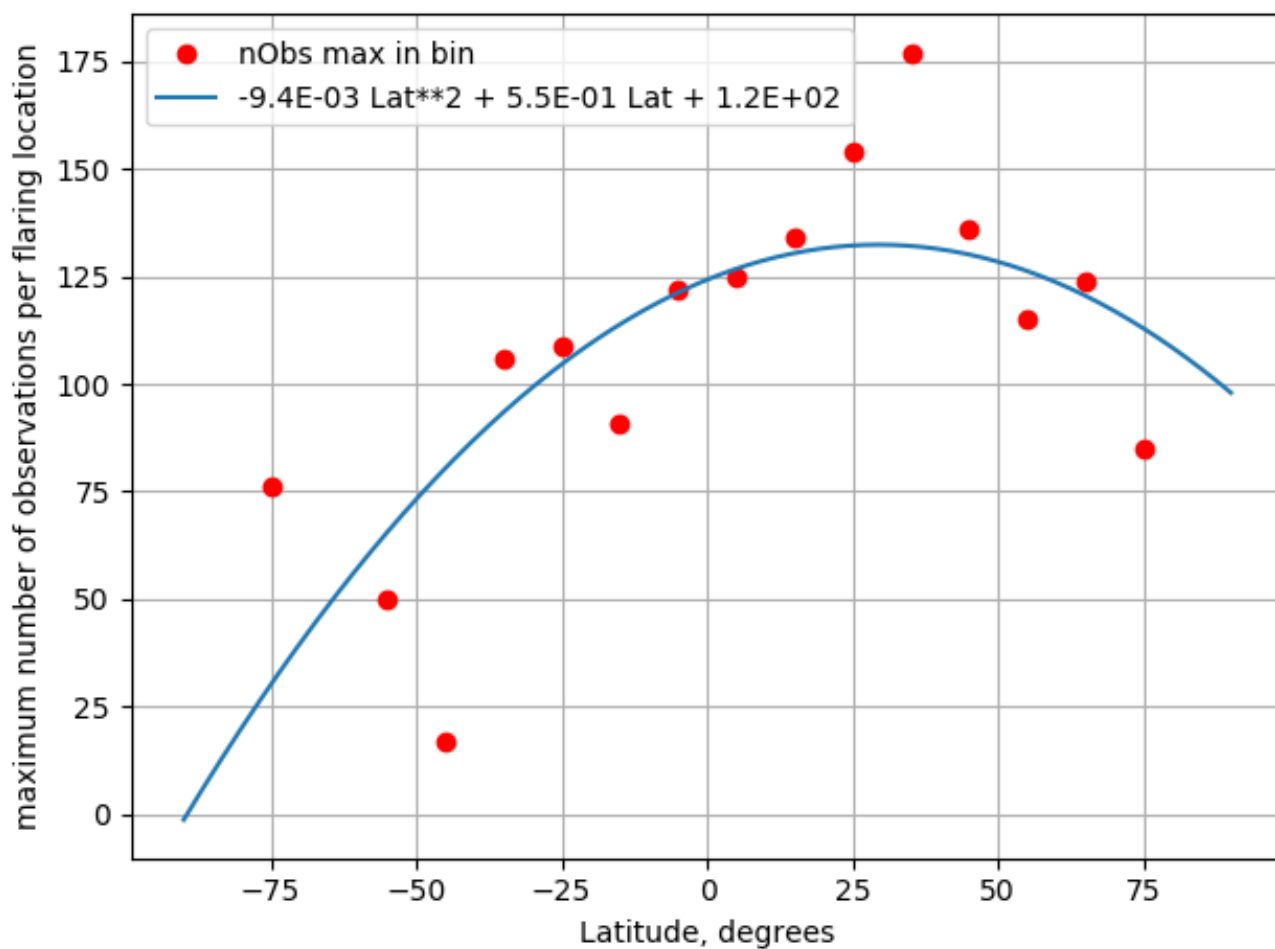
Figure 2. Maximum number of observations per grid cell as a function of Latitude. The latitude values are binned ($10°$). The function expresses the maximum number of observations $n_{Obs_{max}}$, which we assume as a continuous operation of the hot source, as a function of latitude.

For the estimation of the flared volume, we applied the calibration derived by Elvidge et al. (2016) to each single detection within a flaring location grid cell. The calibration relationship uses a modified formulation of the radiative power to output the yearly flared volumes (in Billion Cubic Meters, BCM), which is then scaled to a daily activity in m^3.

The best activity estimate corresponds to assuming that the flare is active for n_{Ops} days:

$$BCM_{best} = BCM_{min} \times \frac{n_{Ops}}{n_{Obs}} \tag{4}$$

The lower bound BCM_{min} for the activity estimate assumes that the flare is only active on the n_{Obs} days with hot spot detections. The upper bound for the activity estimate assumes that the flare is constantly active:

$$BCM_{max} = BCM_{min} \times \frac{365}{n_{Obs}} \tag{5}$$

The emissions of black carbon (BC) from gas flares are estimated using reported emissions factors (EF). Stohl et al. (2013) used an EF of 1.6 $g.m^{-3}$, while Schwarz et al. (2015) and Weyant et al. (2016) conducted field experiments in the Bakken formation (USA) and derived EFs of 0.57±0.14 $g.m^{-3}$ and 0.13±0.36 $g.m^{-3}$ (using the Single Particle Soot Photometer) or 0.28 $g.m^{-3}$ (using the Particle Soot Absorption Photometer), respectively. However, flared gas has not the same composition everywhere and Huang and Fu (2016) considered the regional variability of the EF. The authors applied the function which relates EF to the volumetric gas heating value derived in the laboratory by McEwen and Johnson (2012) to globally compiled gas composition data. Klimont et al. (2017) considered, for the Greenhouse Gas – Air Pollution Interactions and Synergies (GAINS) model, the EF derived by Schwarz et al. (2015) of 0.57 $g.m^{-3}$ for well-operated flares (i.e. Organisation for Economic Co-operation and Development (OECD) countries) and a maximum of 1.75 $g.m^{-3}$ for other countries. In the present work, we apply the same concept of a varying EF but use the flare temperature as an indication of the combustion completeness, instead of the country of origin as an indication of the flare operation. Flaring temperatures close to the adiabatic flame temperature for natural gas (around 2500 K) are associated with more complete combustion and therefore lower BC emissions. On the other hand, low flaring temperatures (700 K and below) are associated with higher BC emissions. Between the two extremes, the BC emission is scaled linearly as a function of the flaring temperature (see Figure 3). To the best of our knowledge, this is the first time that operating practices are taken into consideration when assigning the EF.

The country-level BCM and BC estimates are computed by summing the individual flares estimates within the borders of each country and its exclusive economic zone.

With this methodology we estimate a wide range of possible activity (BCM) and emissions (BC), where our best estimate falls between the 'flaring only when there is a detection' (BCM_{min} and BC_{min}) and 'always flaring' (BCM_{max} and BC_{max}). We conservatively assume that this range of possibilities represents $6 \times \sigma$, and report the uncertainty of the best estimates as $1 \times \sigma$.
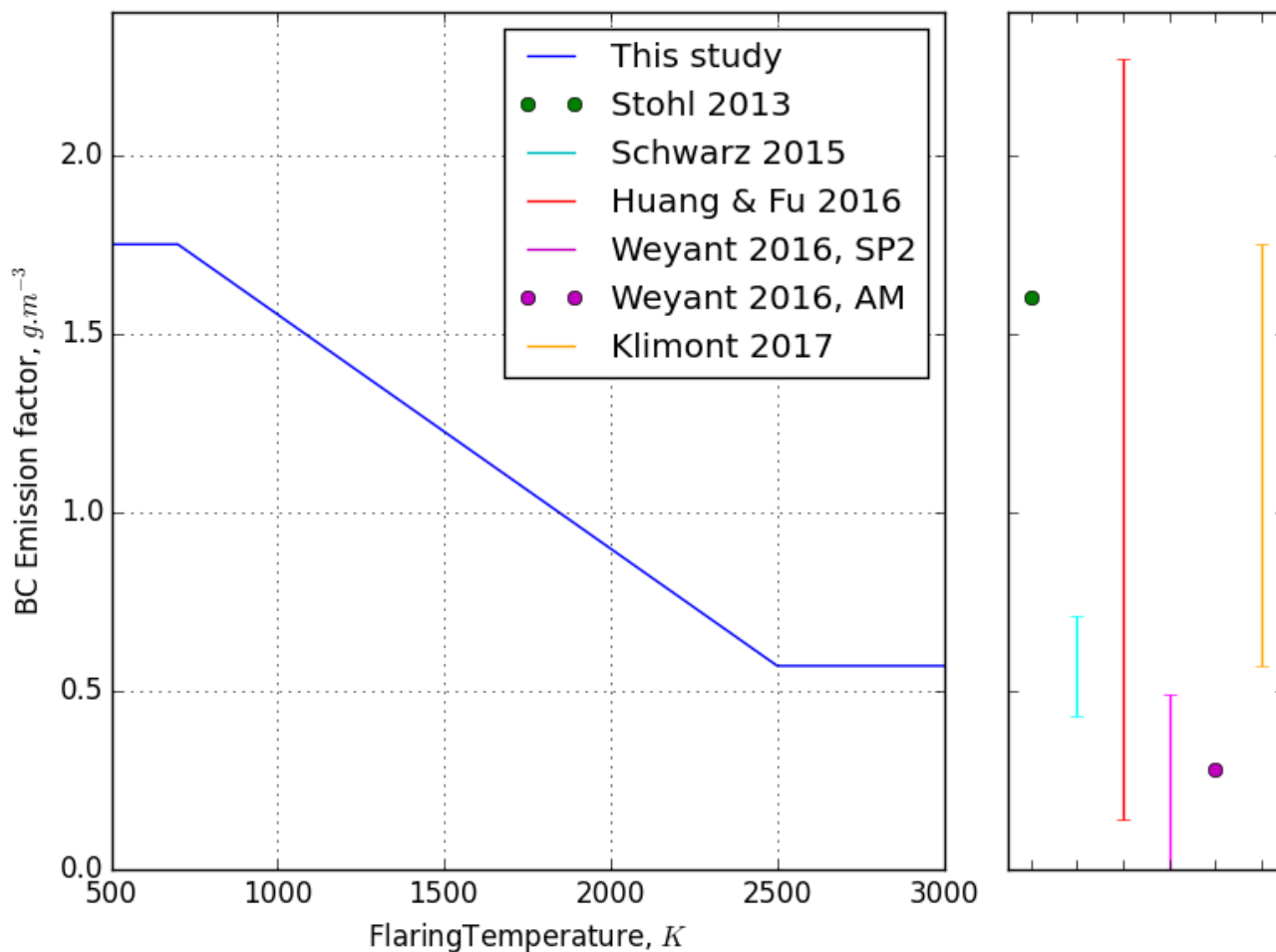
Figure 3. Left: BC emission factor function used in the present study. The emission factor is bounded by the extremes of the range used in the GAINS model (Klimont et al., 2017) and scaled as a function of the flaring temperature, used as an indication of combustion completeness. Right: For comparison purposes, the EFs derived by Stohl et al. (2013); Schwarz et al. (2015); Huang and Fu (2016), Weyant et al. (2016) (using the Single Particle Soot Photometer, SP2, or the Particle Soot Absorption Photometer, AM) and Klimont et al. (2017).

Earth System
**Science
Data**
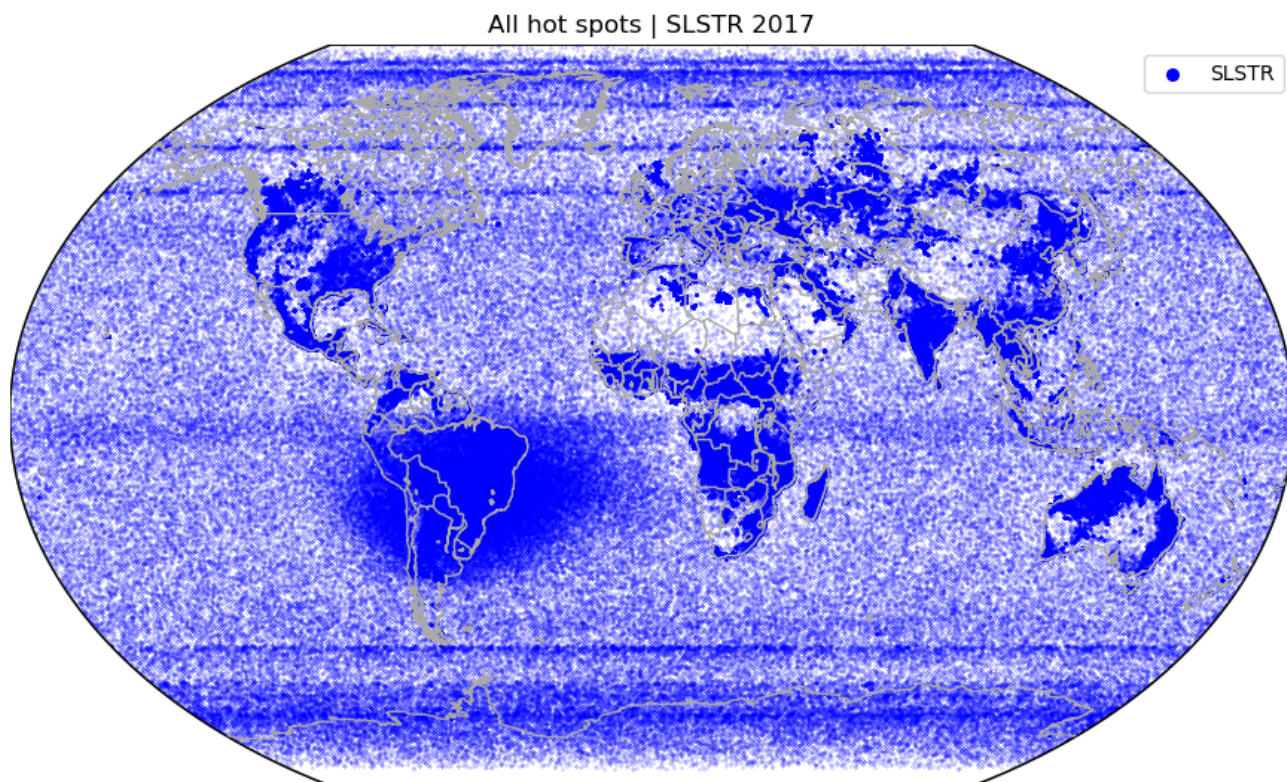
Figure 4. Location of all the 807327 hot spots (all detections database filtered for spurious signals, see Figure 1), detected in 2017.

3 Results

3.1 Hot spots and flaring sites

All the hot spots detected globally for 2017 using the algorithm as described in Figure 1 are shown in Figure 4. The data is available online at the ECCAD webpage (Caseiro and Kaiser, 2019). The algorithm detected 807327 hot spots.

5   Noise, such as detections in the open ocean and the South Atlantic anomaly, is filtered out when considering only the high-accuracy hot spots as defined by Caseiro et al. (2018). There are 95906 high-accuracy hot spots in the dataset. These are shown in Figure 5. Their distribution pattern suggests that they encompass a large range of hot sources, such as wildfires, volcanoes and industrial sources.

After gridding, filtering out active volcanoes (our methodology, see Section 2.2.1, accounted for 71 volcanic eruptions in 10   2017) and retaining the grid cells passing the GF criteria (see Section 2.2.2) the number of globally detected flaring sites in 2017 are 6232, see Figure 6. This is lower than the estimate of 7467 by Elvidge et al. (2016). Although our Sea and Land Surface Temperature Radiometer (SLSTR)-based methodology is able to detect smaller gas flares due to the availability of
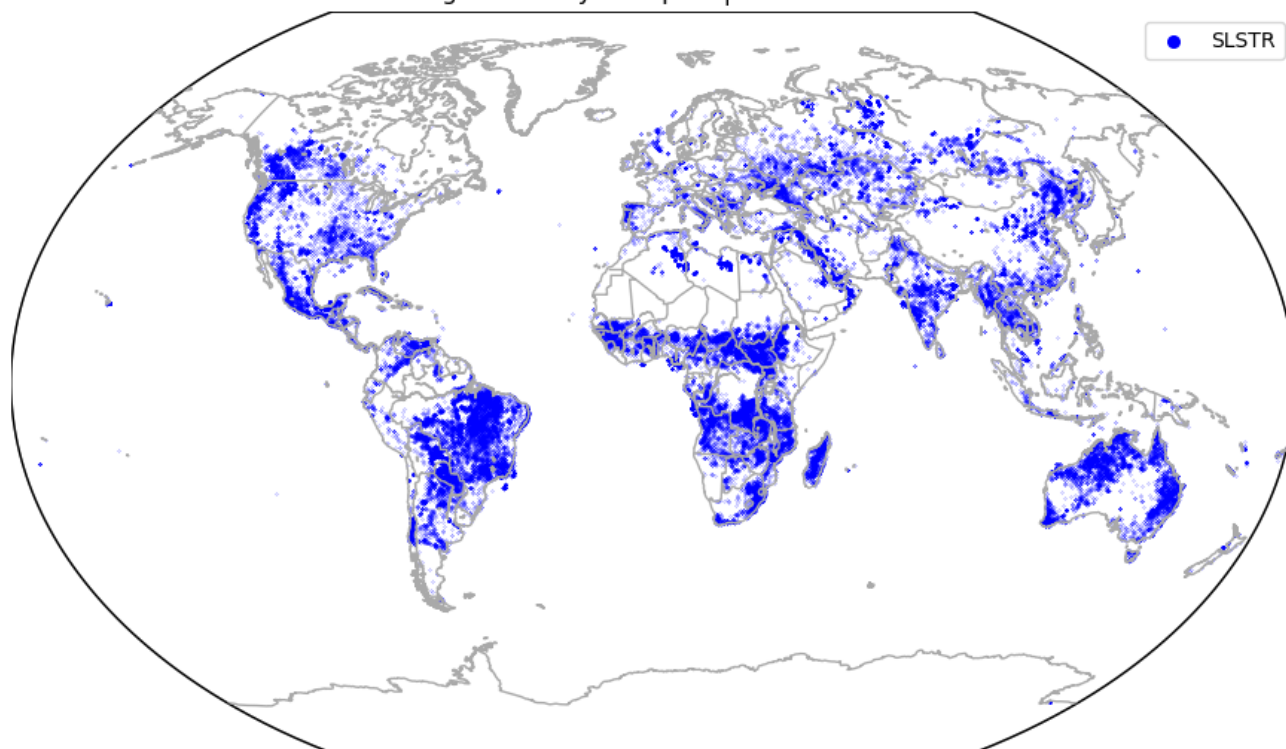
Figure 5. Location of all the 95906 high-accuracy hot spots (gridded hot spots filtered for cloudiness and accuracy of the Planck curve fitting, see Figure 1), detected in 2017.

the second SWIR channel, the Visible Infrared Imaging Radiometer Suite (VIIRS) Nightfire algorithm is expected to detect a larger number of hot spots because it considers local maxima, whereas our methodology clusters adjacent hot pixels.

Russia (985) and the United States (917) are the countries with the highest number of flaring locations. The third country is Iran (441) with less than half of the top two countries. The five countries with more than 300 flaring locations – China (365)

5   and Algeria (324) in addition to the top 3 – account for about one half of the global flaring locations. The United States is the country with the largest difference in the number of flaring locations between 2017 (this work, 917) and 2012 (2399, as reported by Elvidge et al. (2016)). Besides the aforementioned methodological difference, a switch from well-product testing to formal operation could be the reason for a lower number of detected flaring sites (Liu et al., 2018). Such a transition from a higher number of lower intensity flares to a smaller number of higher intensity flares was reported between 2012–2014 and

10   2015–2016 by Franklin et al. (2019) for the Eagle Ford shale region of South Texas.

The time series of the cumulative number of the high accuracy observations for the most active flaring location (in Venezuela, see Section 3.4) is shown in Figure 8. It shows flaring activity throughout the year.
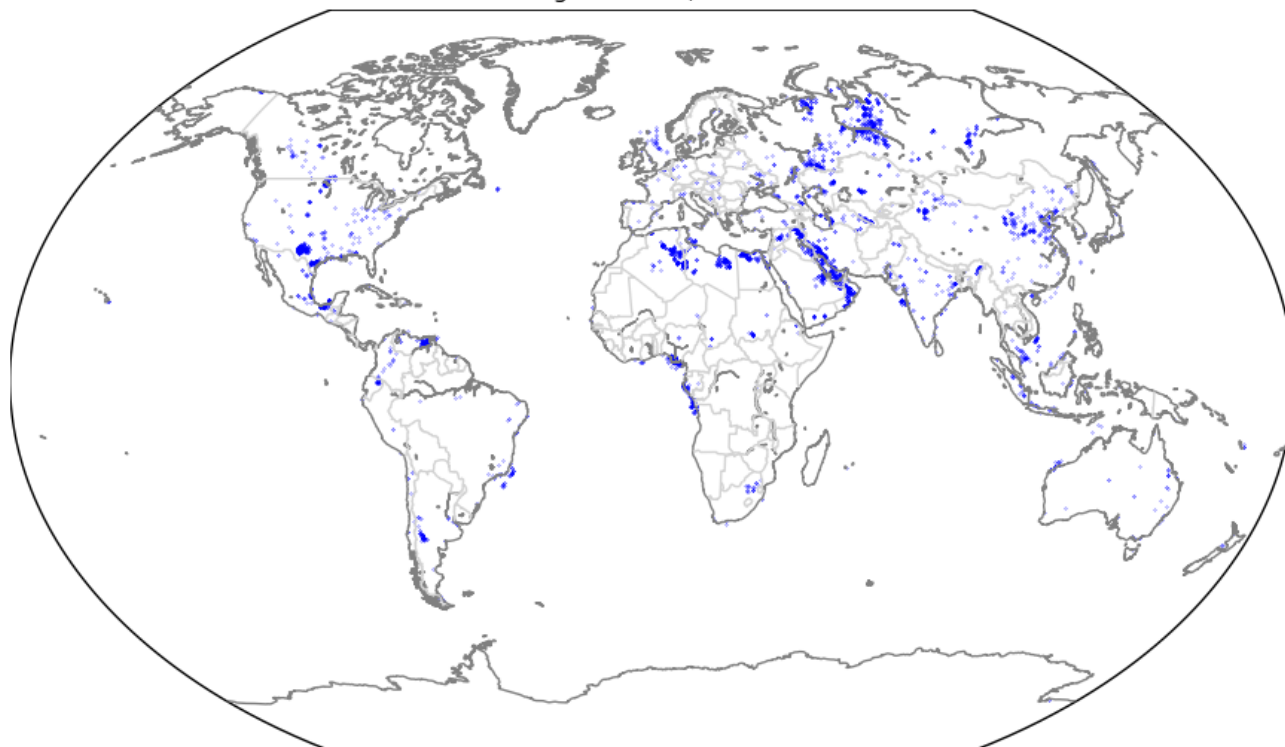
Figure 6. Location of all the 6232 flaring locations (grid cells with at least 5 high-accuracy hot spots and a maximum retrieved temperature above 1500 K) detected in 2017.

3.2 Flaring characteristics

Statistics on retrieved temperature and radiative power are reported in Figures 9 to 13.

The average temperature at the flaring locations approximately ranges from 950 K to 2250 K. This is slightly lower than the range reported by Liu et al. (2018) who used Visible Infrared Imaging Radiometer Suite (VIIRS) Nightfire data, as expected

5   from our previous study (Caseiro et al., 2018). It confirms the bi-modal distribution with modes around 1750 K and 1200 K that is has also been observed by VIIRS.

One of the most active flaring regions of the world is the Persian gulf. Figure 10 shows the average retrieved temperature at flaring locations in that region, while the time series of the retrieved flaring temperatures is shown in Figure 11. The time series of the retrieved temperature for the most active flaring location (in Venezuela, see below, section 3.4) is shown in Figure 12.

10   The average radiative power at flaring locations range from a few tenths of MW up to approximately 1 GW (Figure 13), spanning the 5 orders of magnitude reported by Elvidge et al. (2016).
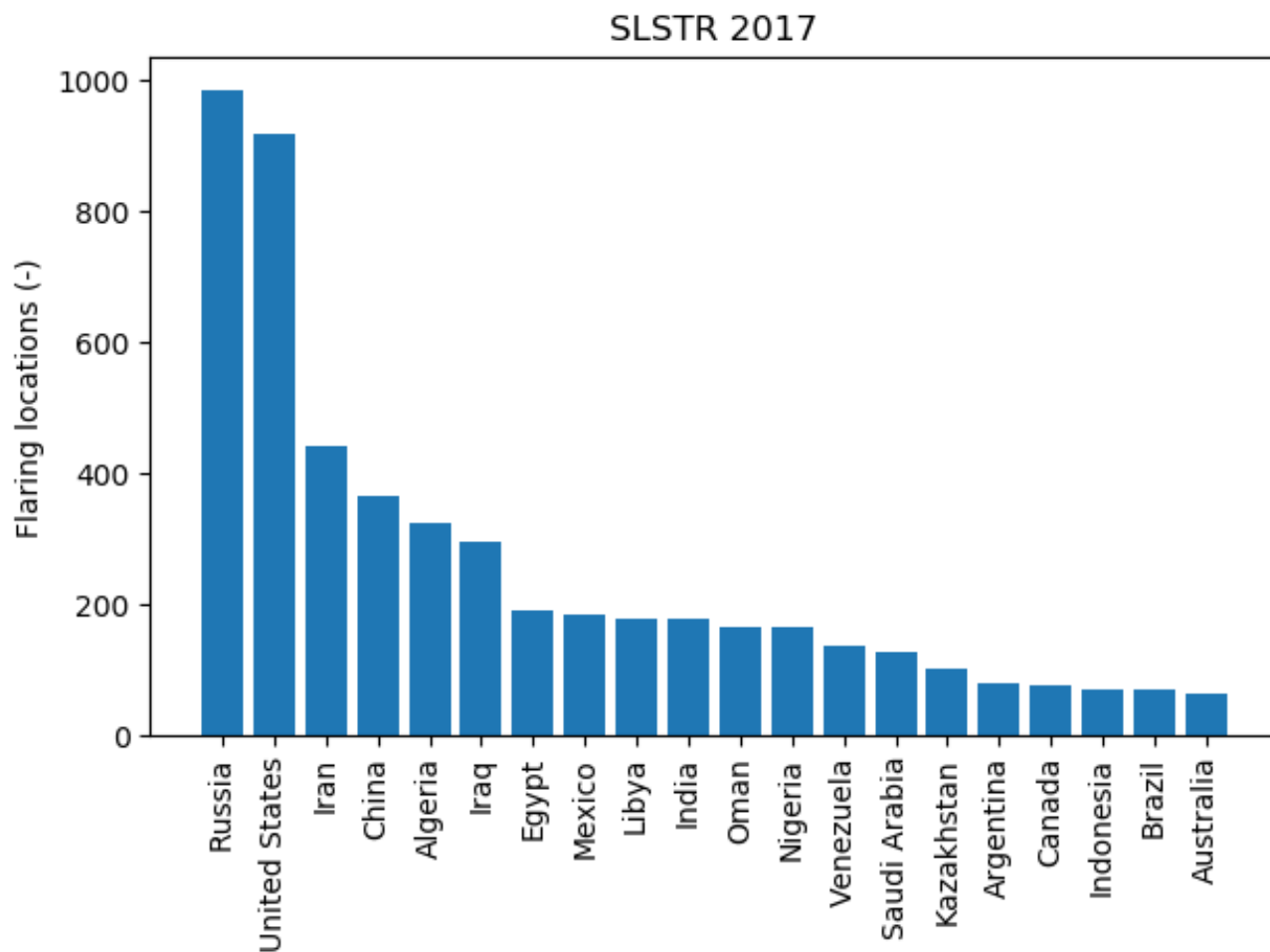
Figure 7. Flaring locations by country, top 20.

3.3 Comparison with VIIRS Nightfire

We compare our results to the data set from the Visible Infrared Imaging Radiometer Suite (VIIRS) Nightfire 2017 results made available by the National Geophysical Data Center of the National Oceanic and Atmospheric Administration of the United States at https://www.ngdc.noaa.gov/eog/viirs/download_viirs_fire.html. Figure 15 shows all Nightfire detections in 5 2017 (green), projected onto the same $0.25° \times 0.25°$ global grid as for our results (see above, sections 2.2.2 and 3.1).

In order to segregate the flaring signal from other hot spots, we adapt the thresholds we used for hte Sea and Land Surface Temperature Radiometer (SLSTR). The persistency threshold was adjusted from 5 (for a 1400 km swath for SLSTR) to 11 detections a year within a grid cell (for a 3040 km swath for VIIRS). The lowest yearly maximum temperature retrieved within a grid cell was maintained at 1500 K. Grid cells which comply to these criteria are shown in Figure 15 (red). These adapted
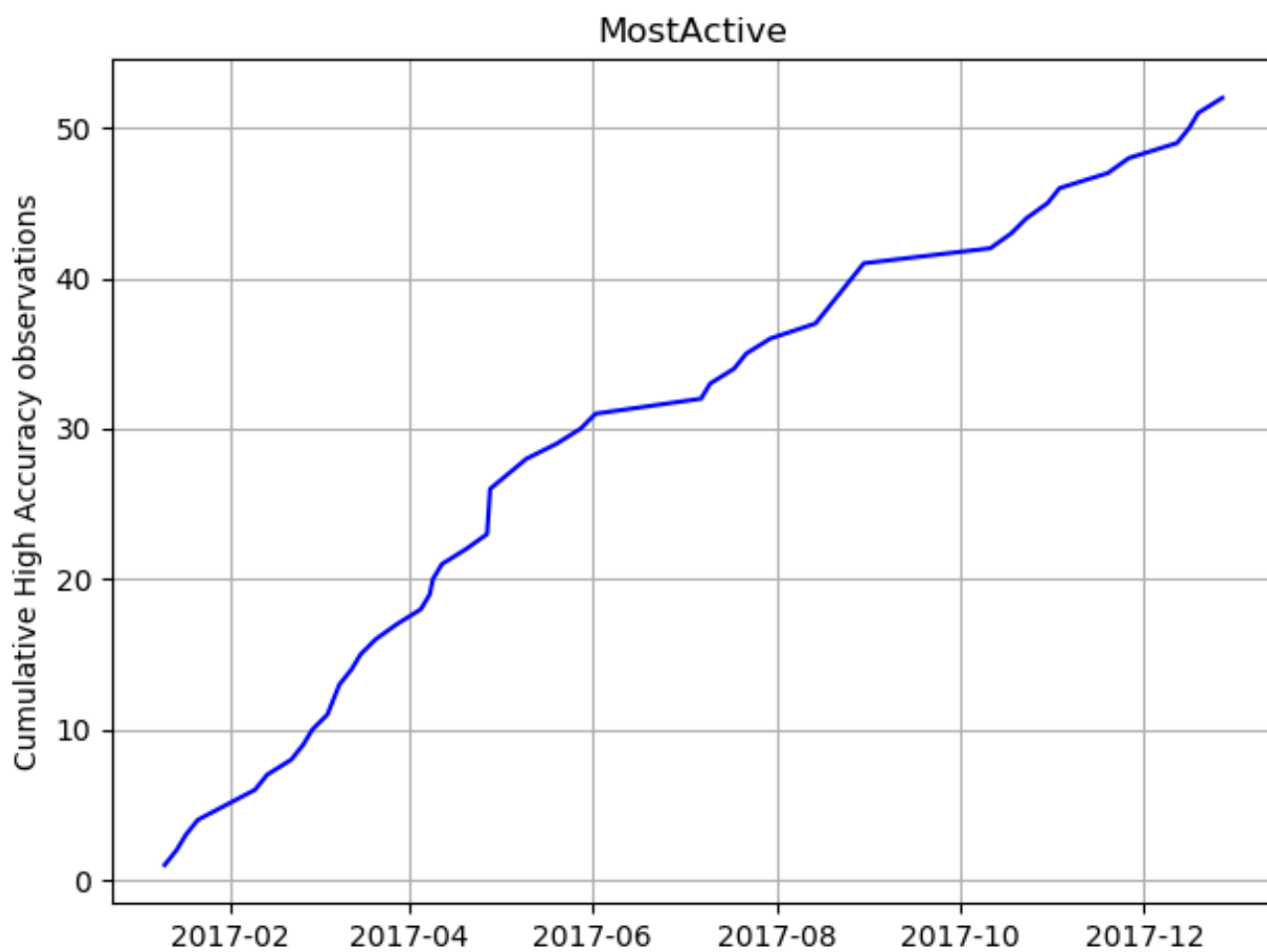
Figure 8. Cumulative number of high accuracy observations at the most active flaring location (52 high accuracy detections over 47 days at the grid cell centered at 63.6875°W, 9.6375°N).

Earth System
Science
Data
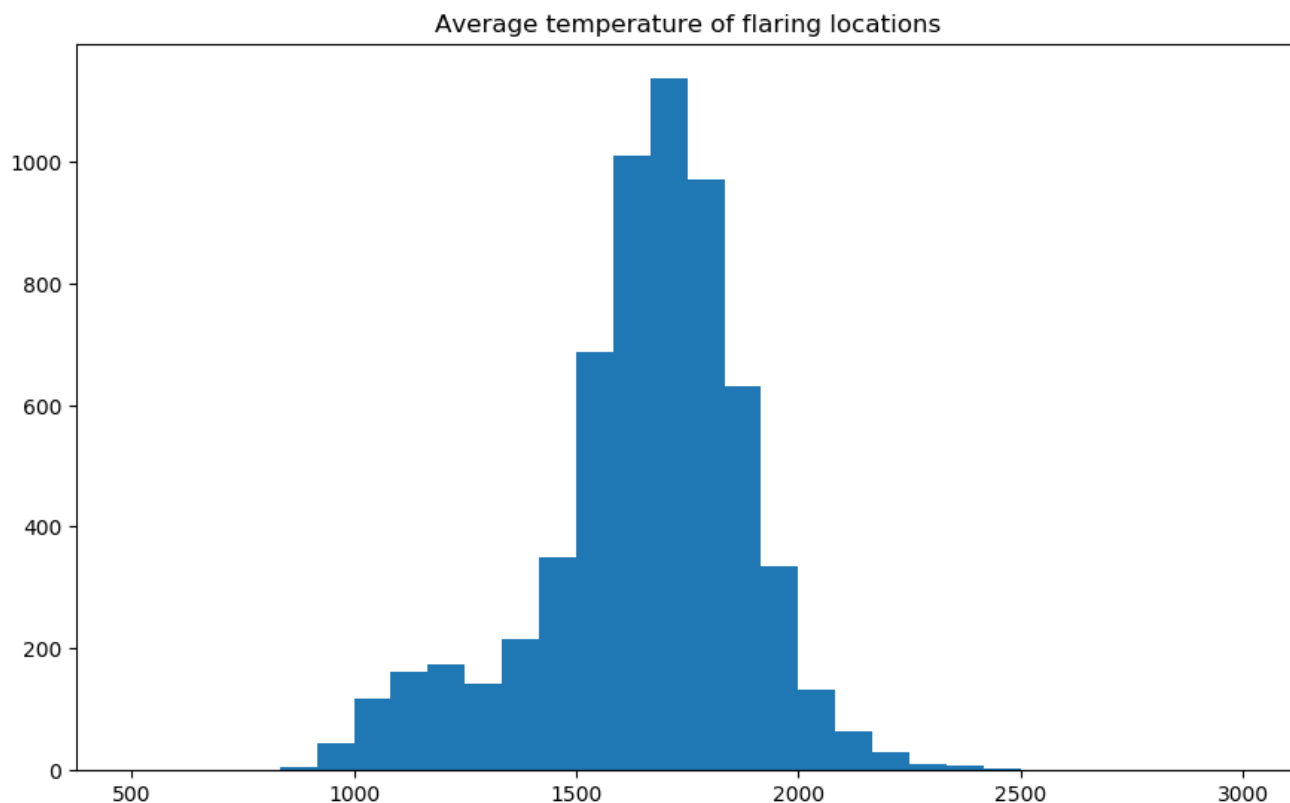
Figure 9. Distribution of the average retrieved hot spot temperature (K) for the flaring locations.

thresholds filter out a very large number of hot spots and produce a global VIIRS Nightfire flaring map similar to that obtained by our methodology based on SLSTR observations (see Figure 6). Despite this global agreement, some significant regional differences are visible: the Western U.S. and Canada, the Amazonian forest, Australia, Eastern and Western China. Liu et al. (2018) referred to this last region as "undetected oil/gas heat source" in Elvidge et al. (2016). The number of detected VIIRS

5 Nightfire flaring locations (18855) is about three times that returned by our methodology (6232). Such a behaviour is expected because the Nightfire algorithm considers pixels which are local maxima and our methodology aggregates contiguous hot pixels within a same cluster. These clusters may be very large and contain more than one local maximum.

The distribution of the retrieved average flaring temperatures at each site is very similar, as shown in Figure 16.

3.4 Flared volumes

10 The activity for all the individual flaring locations is shown in Figure 17. The distribution is very close to that reported by Elvidge et al. (2016), with the exception of the very few extremes in the range 0.8–1.1. The most active flare burned 0.623 BCM throughout 2017 and is located south of Punta de Mata in Venezuela. This is also where Elvidge et al. (2016) found the
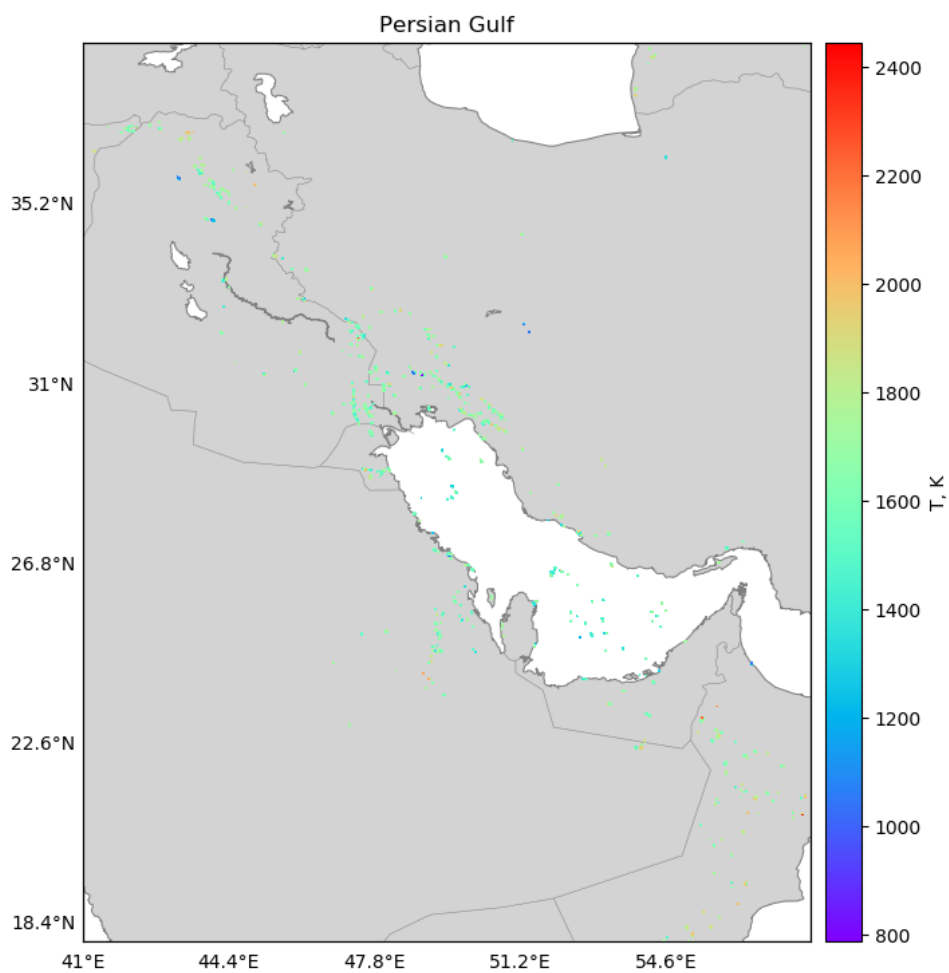
Figure 10. Average flaring temperature (K) at flaring locations in the region of the Persian gulf (1184 flaring locations in the region, aggregated from 41600 high-accuracy detections over 348 days).
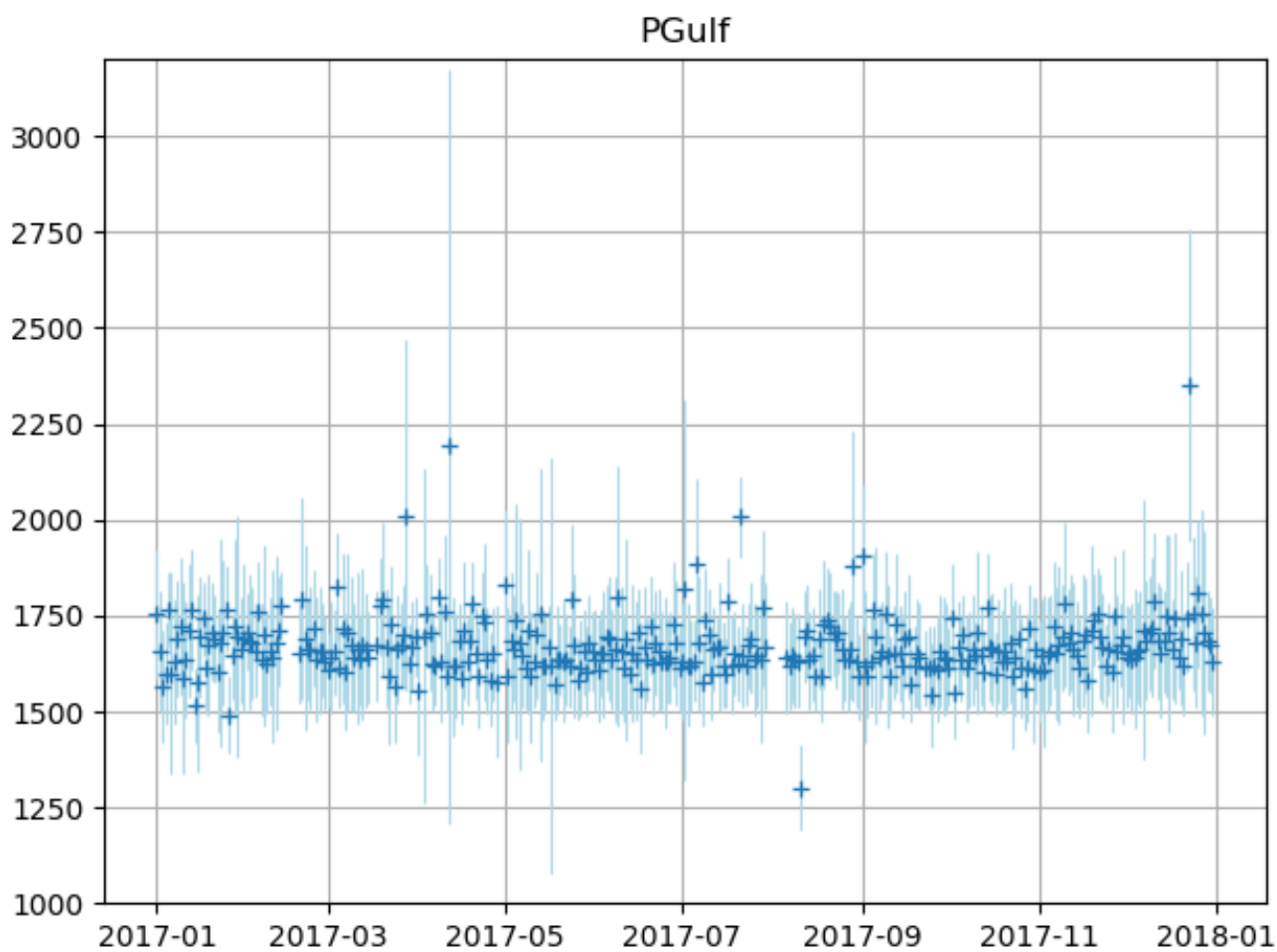
Figure 11. Time series of the daily average retrieved flaring temperatures (K, the bounds represent 1 standard deviation) in the region of the Persian gulf (41600 high accuracy detections over 348 days at 1184 flaring locations) shown in Figure 10.
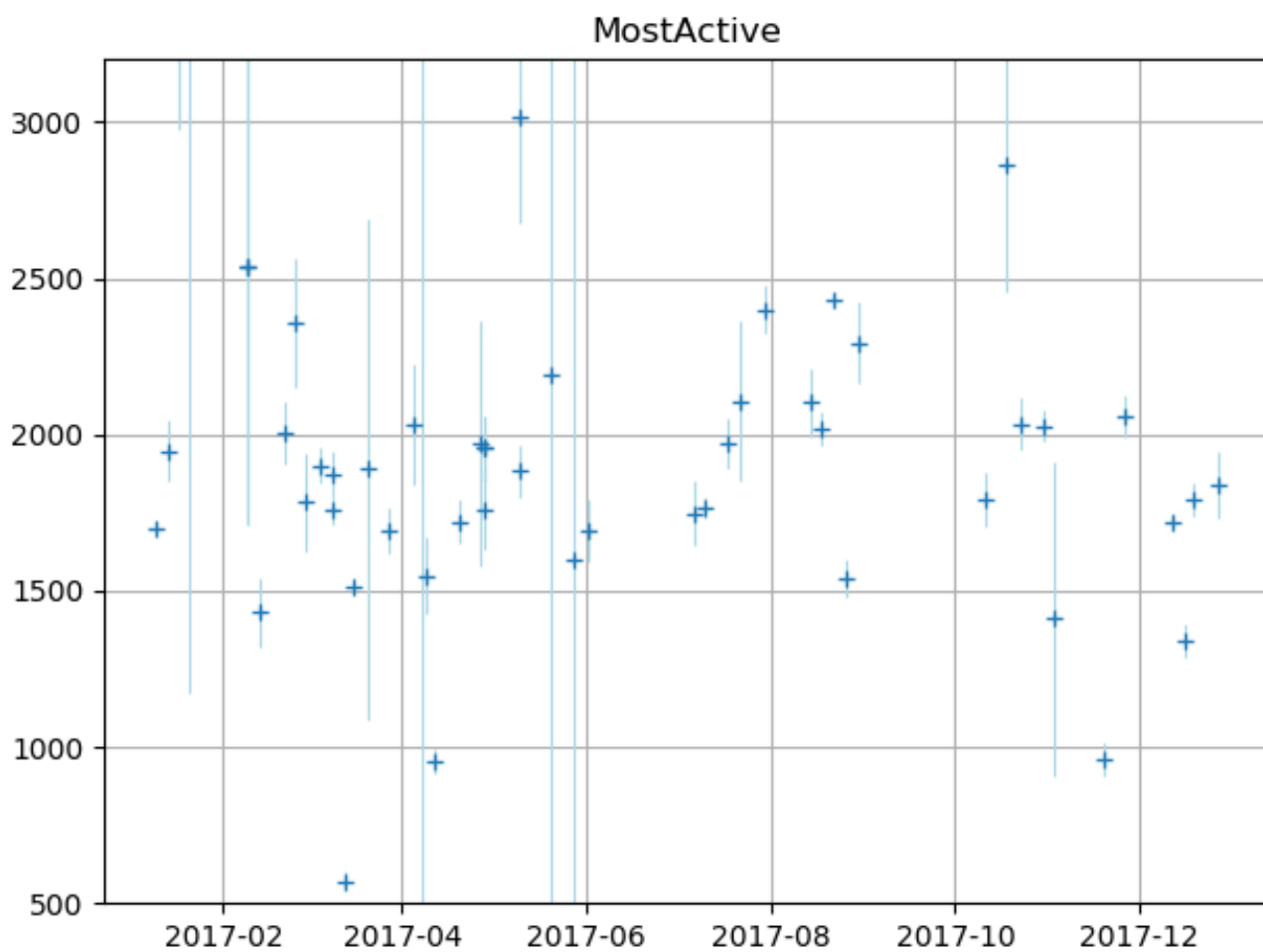
Figure 12. Time series of the retrieved temperatures (with bounds) at the most active flaring location (52 high accuracy detections over 47 days at the grid cell centered at 63.6875°W, 9.6375°N in Venezuela).
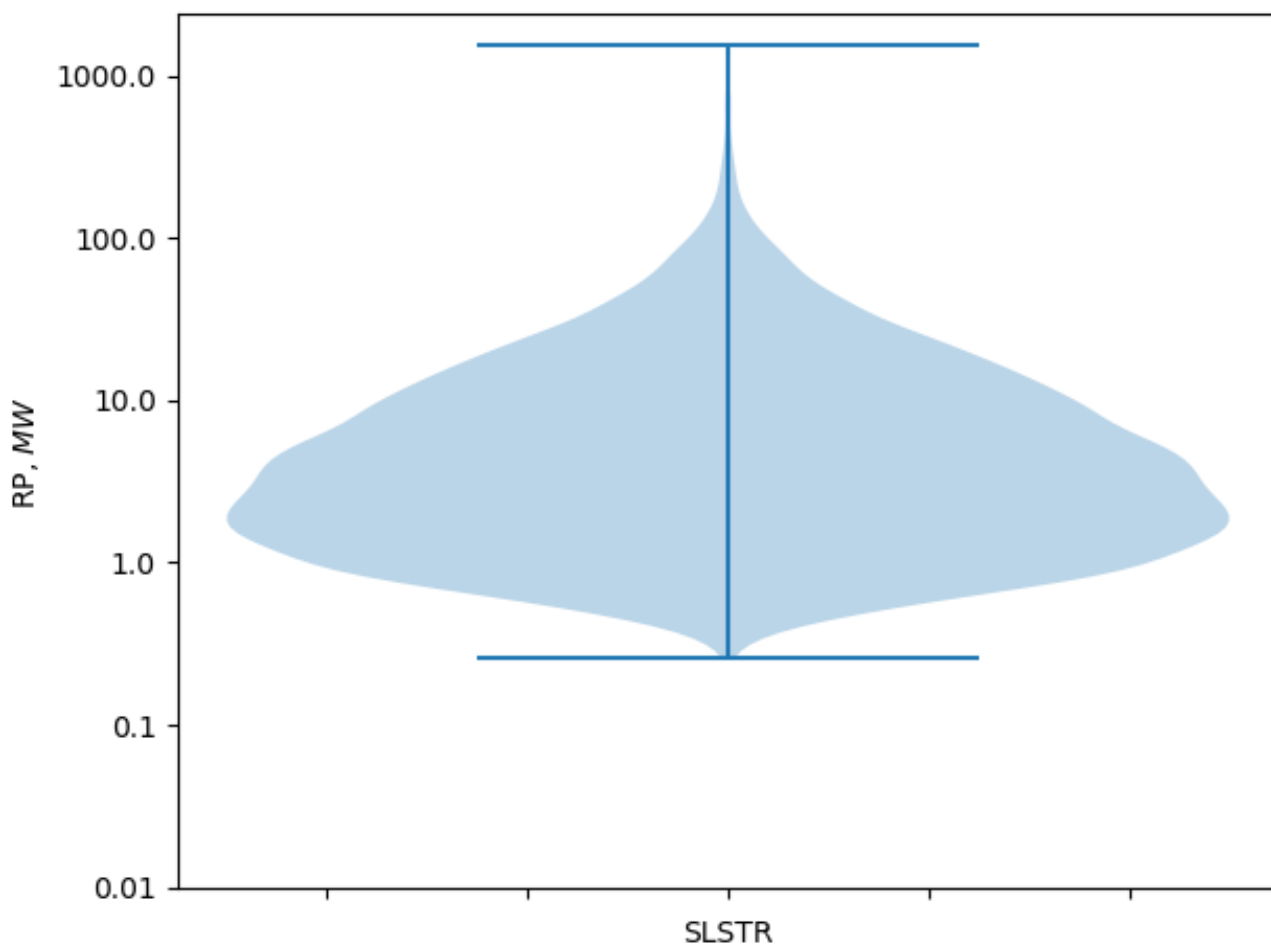
Figure 13. Distribution of the average radiative power (MW) for the 6232 global flaring locations.

most active flare for 2012, though more active (1.13 BCM). The total activity of the region is shown in Figure 18, and the cumulative activity throughout the year in Figure 19.

Our best estimate for the global flared volume for 2017 is 129±64 BCM. This is slightly lower than the 143±13.6 BCM reported by Elvidge et al. (2016) for 2012. The lower and upper bounds of the range of possibilities for the estimate are 35.0 BCM (there is flaring only when there is a detection) and 419.1 BCM (flaring is always on), respectively.

Approximately half of the global flared volume originates from 4 countries only: Iraq (19.0 BCM), Iran (18.4 BCM), Russia (18.1 BCM) and Algeria (10.5 BCM).
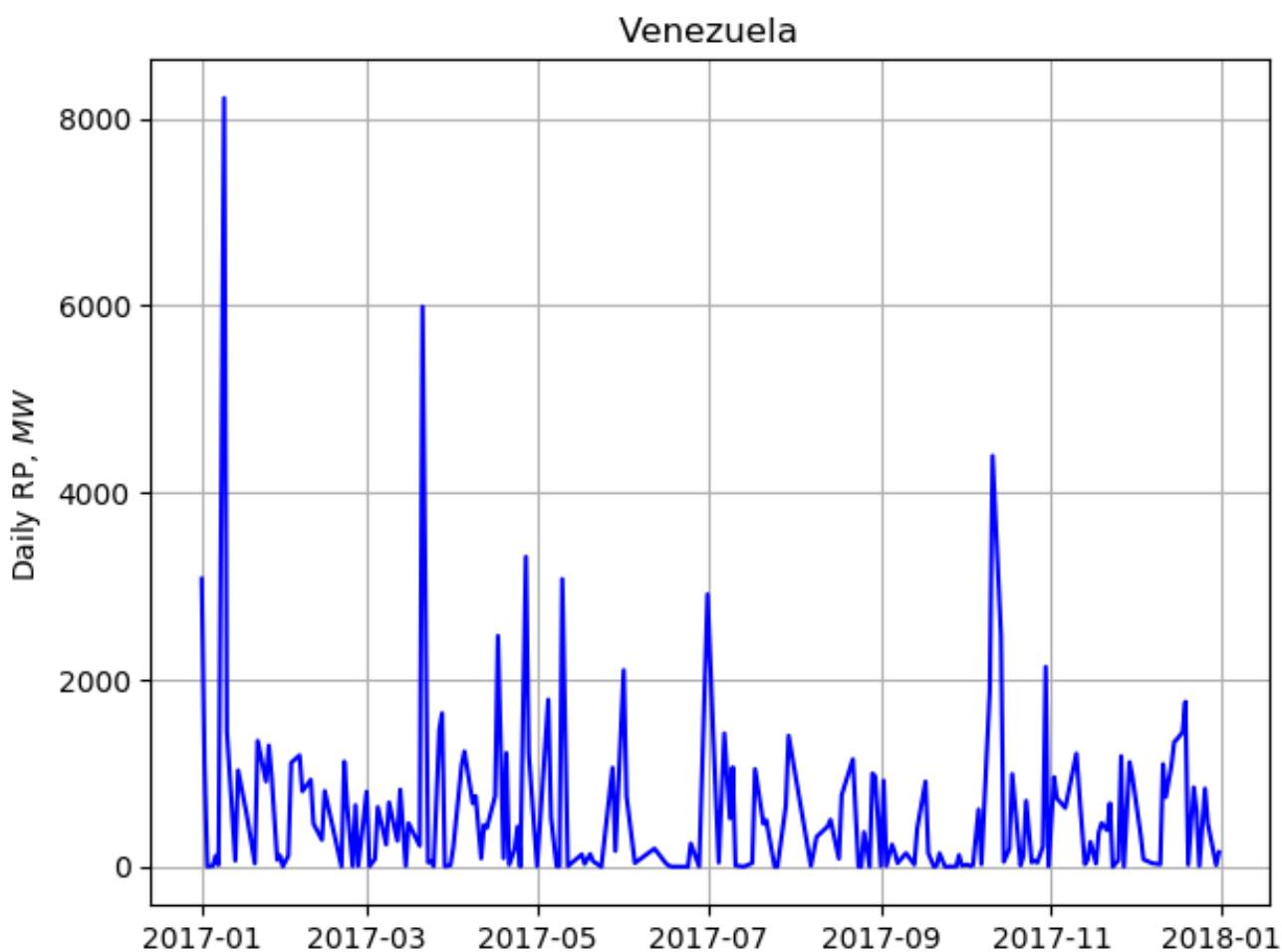
Figure 14. Time series of the total radiative power (MW) in the oil producing region of Venezuela (2391 high accuracy observations at 112 flaring locations over 200 days), where the most active flare is located (see below, section 3.4).
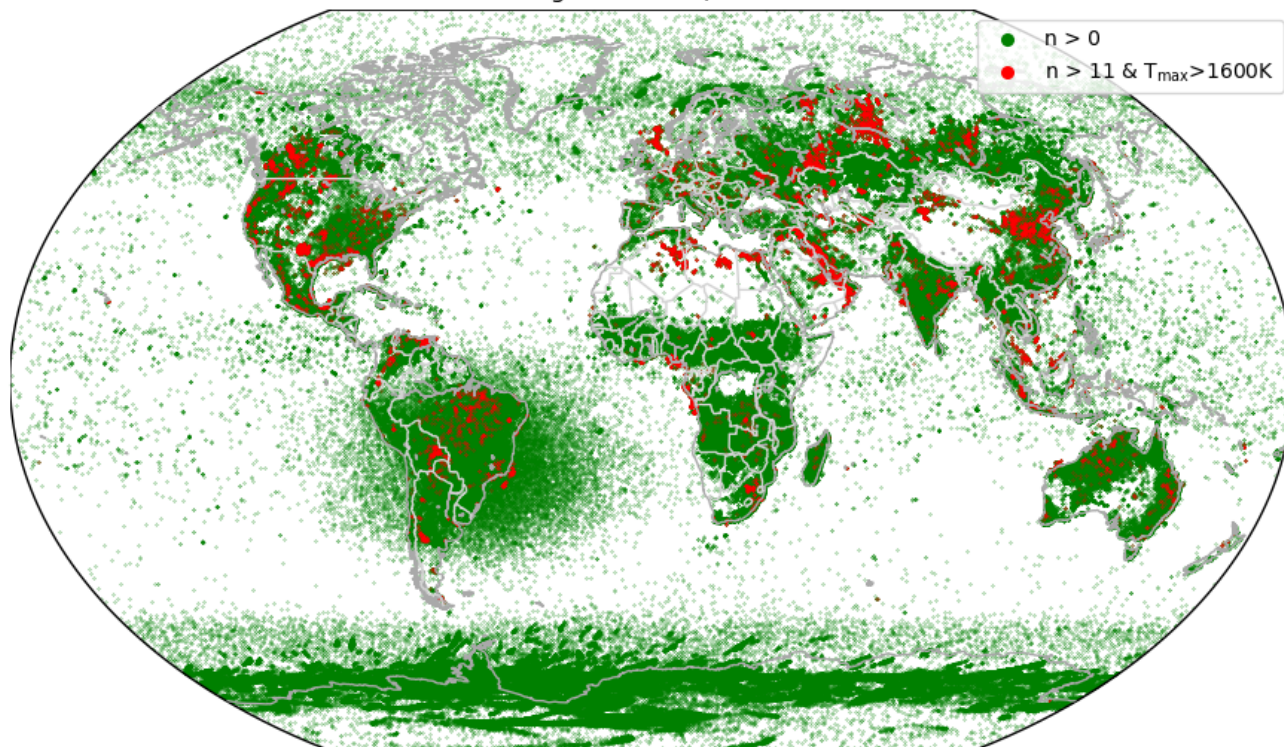
Figure 15. VIIRS Nightfire locations (all locations, green, and flaring locations, red) for 2017. The flaring locations were derived by adapting our SLSTR flaring location thresholds to the VIIRS sensor characteristics: at least 11 detections within the grid cell and at least 1600K as the maximum temperature detected within the grid cell.

3.5 BC emissions

The black carbon (BC) emissions for all the individual flaring locations are shown in Figure 21. The most active flare emitted 0.35 Gg BC in 2017 (south of Punta de Mata). The cumulative BC emissions throughout the year for the whole Persian gulf region is shown in Figure 22.

5   Our best estimate for the global BC emissions from gas flaring is 73.4±36.7 Gg. As for the flared volume, 4 countries account for more than half of that value: Iraq (10.8 Gg), Iran (10.5 Gg), Russia (10.3 Gg) and Algeria (6.0 Gg). This value is about one third of the estimate from the Greenhouse Gas – Air Pollution Interactions and Synergies (GAINS) model (ECLIPSE V5a global emission fields) (Klimont et al., 2017): 270 and 210 Gg in 2005 and 2010, respectively. Such a decrease between 2010 and 2017 may be unlikely, given that the production within the upstram oil and gas (UOG) industry did not decrease in

10   such a significant way. Rather than a decrease in the activity, or a shift in the emission factors (EF), the discrepancy might be due to how the EF is determined (see section 2.3). Assigning the EF at the operational level, for each detection, seems to us
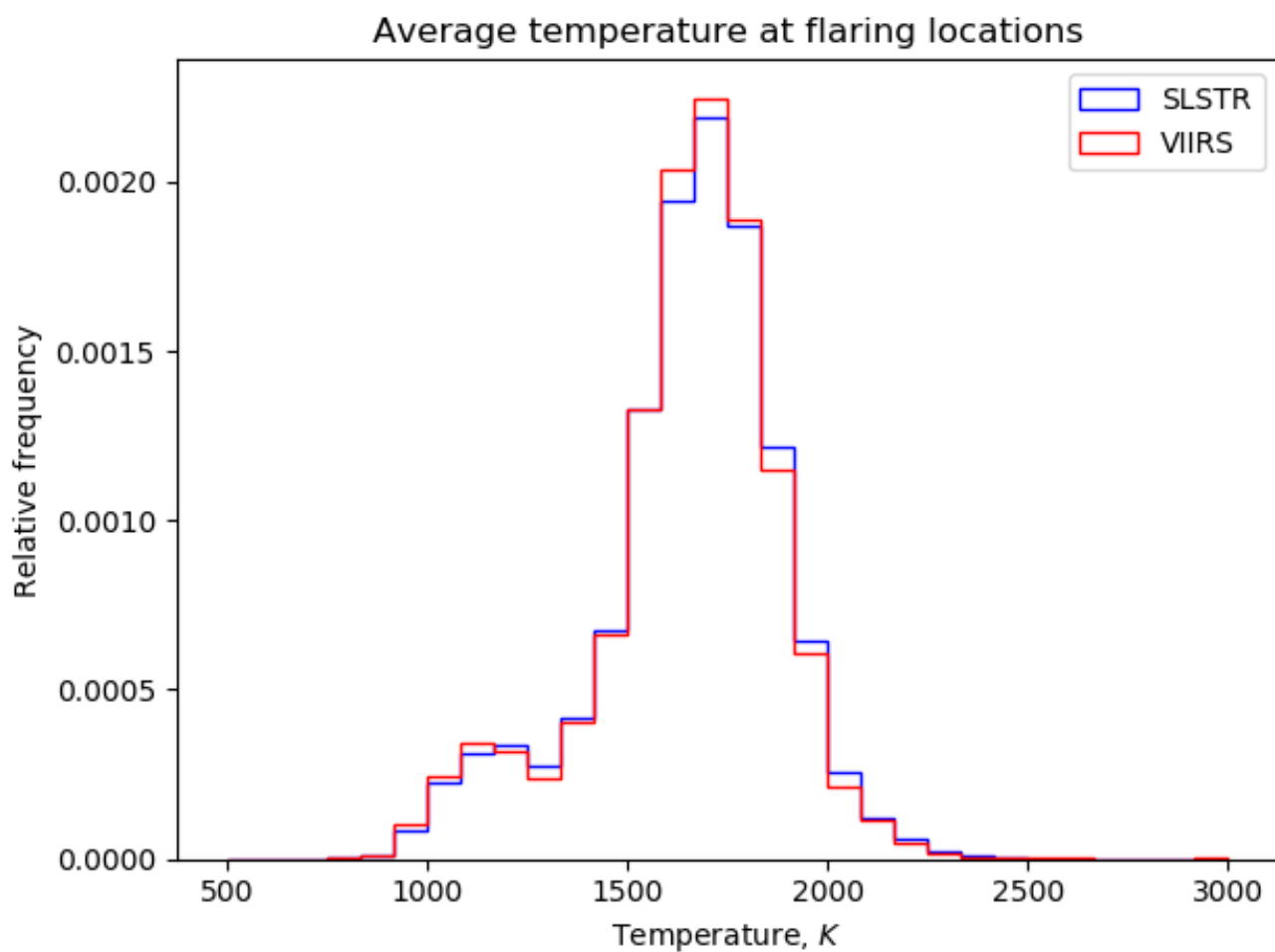
Figure 16. Comparison of the average retrieved temperature at the flaring locations for VIIRS Nightfire (locations shown in Figure 15 in red) and for SLSTR (locations shown in Figure 6 in blue). Relative frequency is used to ensure comparability independently of the total number of observations (6232 flaring locations for SLSTR, 18855 flaring locations for VIIRS Nightfire).
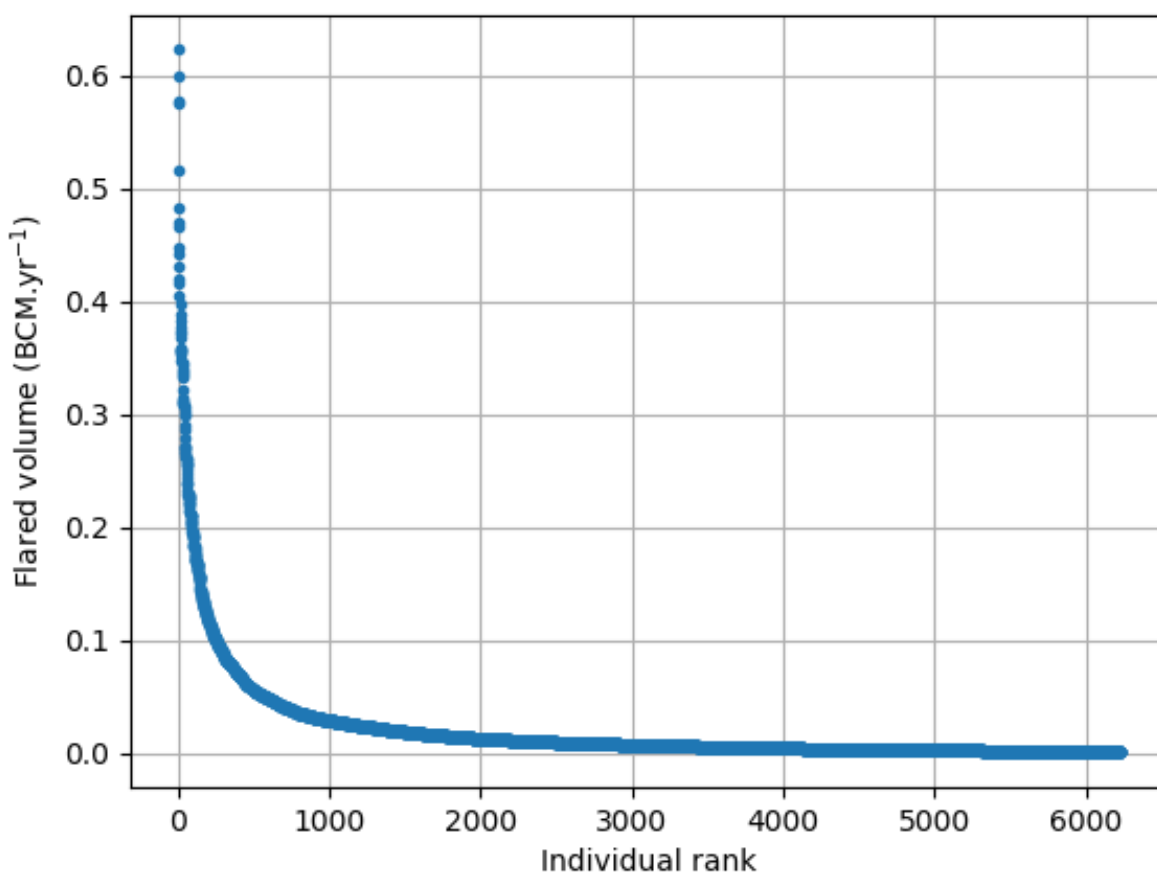
Figure 17. Flaring activity (best estimate, BCM per year) for each individual flaring location (6232 in total).

more realistic than assigning it at the country level. Our global estimate is also larger than the global extrapolation made from a flaring emission study in the Bakken field by Weyant et al. (2016): 20±6 Gg. We believe that our dynamic assignment of the EF, based on the single temperature retrieval, should be closer to reality than globally extrapolating the EF measured at a single field. Huang and Fu (2016) used the VIIRS Nightfire dataset for the flaring activity and emission factors derived from the flared gas chemical composition to compute the BC emissions. Their estimate range from approximately 140 and 200 Gg per year between 1994 and 2012. VIIRS Nightfire was also the basis for the determination of atmospheric emissions from gas flaring by Doumbia et al. (2019) for the African continent. The authors computed a BC emission in 2005 between 6.2 and 141.2 Gg. For the same continent, our results yield 16.1 Gg.
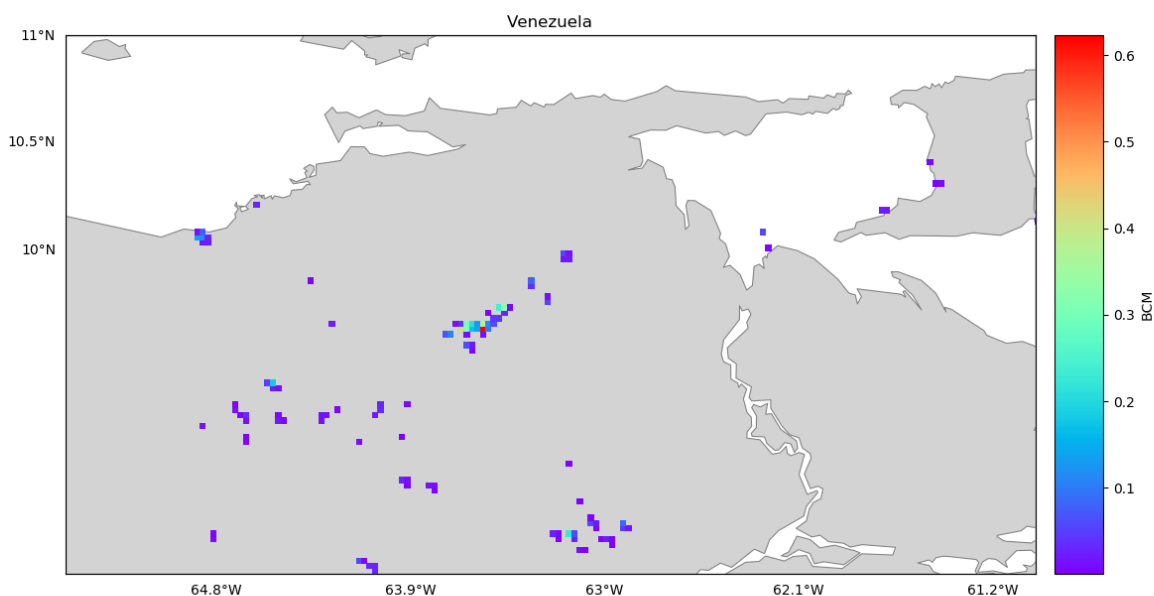
Figure 18. Total flaring activity (best estimate, BCM per year) for each individual flaring location in the oil producing region of Venezuela (112 flaring locations in the region, aggregated from 2391 high accuracy detections over 200 days), where the most active flare is located.

4 Conclusions

In this work we apply a previously described hot spot detection and characterisation procedure (Caseiro et al., 2018) to the 2017 observations of Sentinel-3A's Sea and Land Surface Temperature Radiometer (SLSTR) instrument. We present a new gas flaring discrimination procedure, based on two characteristics of gas flares: persistence and temperature. This allow us to

5 refine the characterisation procedure in order to separate gas flares from other sources of heat emissions. Validation through referencing with high-resolution images yields a detection accuracy of 85±11%, with a commission error of 3±1%.

Our methodology detects 6232 flaring sites worldwide in 2017. Over half of those are located in five countries only: Russia, the United States, Iran, China and Algeria.

Additionally to the detection we present a way to assess the volume of flared gas. This is based on the observed relationship

10 between the flared volume and observed flare radiative energy. The resulting estimate of flared volume allows us to estimate activity from which we can infer emission estimates.

In order to compute the best estimate of activity at the detected flaring sites, we apply a scaling factor, differentiated by latitude, to account for observation gaps (cloud cover and overpass frequency). The upper bound is computed as if the flare would constantly burn for the whole year. The lower bound is computed as if the flare would burn on days with hot spot
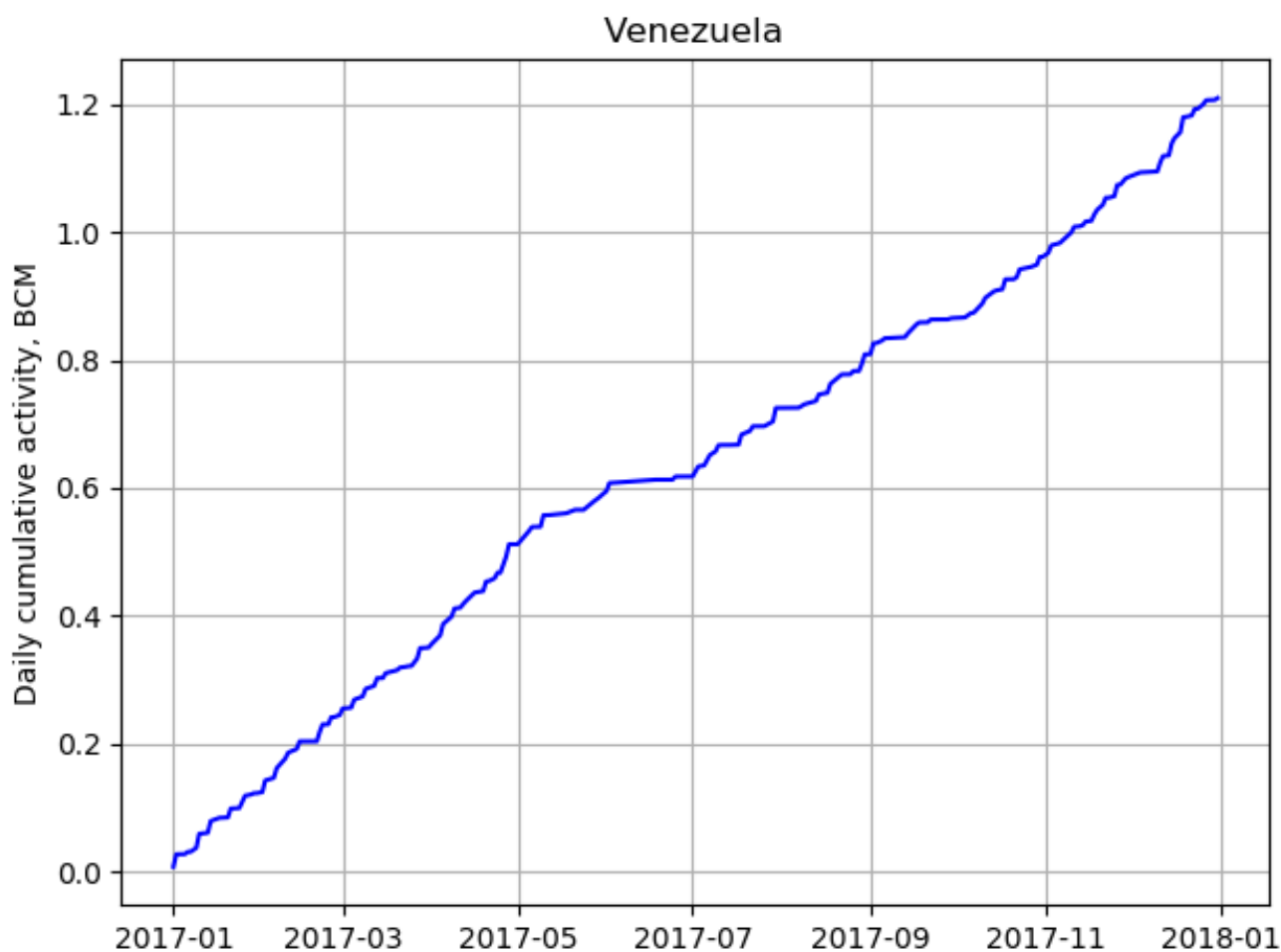
Figure 19. Cumulative total observed flaring activity (BCM_{min}) in the oil and gas producing region of Venezuela (112 flaring locations in the region, aggregated from 2391 high accuracy detections over 200 days), where the most active flare is located.
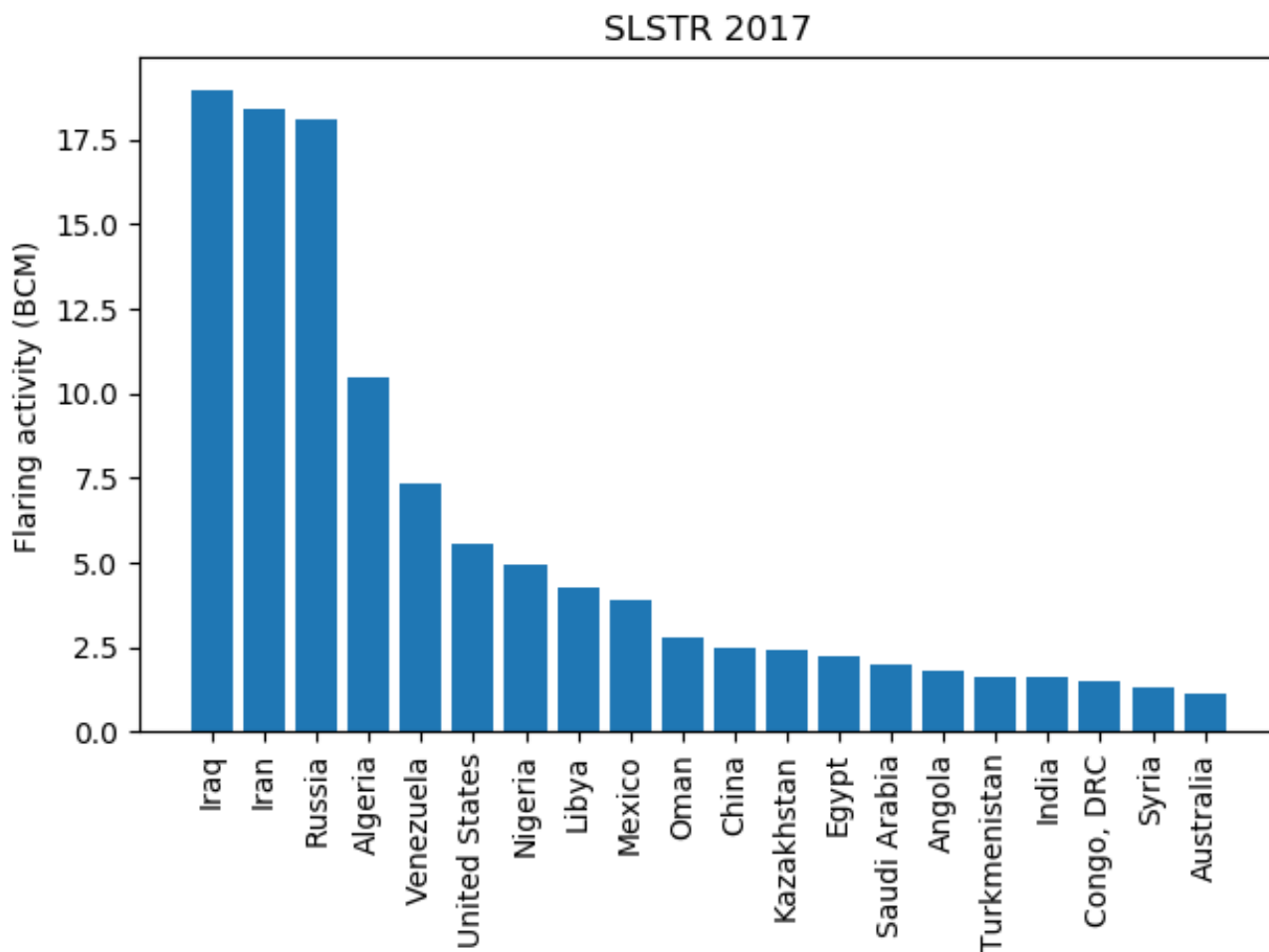
Figure 20. Flaring activity (best estimate, BCM per year) by country, top 20.

detections only. Our analysis yields a result of 129±64 billion cubic metres (BCM) of gas flared in 2017 (best estimate). Only four countries are responsible for half of the global gas flaring activity: Iraq, Iran, Russia and Algeria. The most active flaring location is located in Venezuela and burned 0.623 BCM in 2017.

We further quantify the black carbon (BC) emissions due to gas flaring. We assume that temperature is an indication of the completeness of combustion and use the flame temperature as derived by the hot spot detection and characterisation procedure to determine the emission factor for each single detection, bounded by the range of previously published emission factors. We assume that a temperature close to the adiabatic flame temperature corresponds to the lower bound of the emission factor range considered, while the lowest temperature corresponds to the upper bound. The minimum, maximum and best estimates for the BC emissions are computed in the same way as the flared volume. Our resulting best estimate for the emission of BC to the
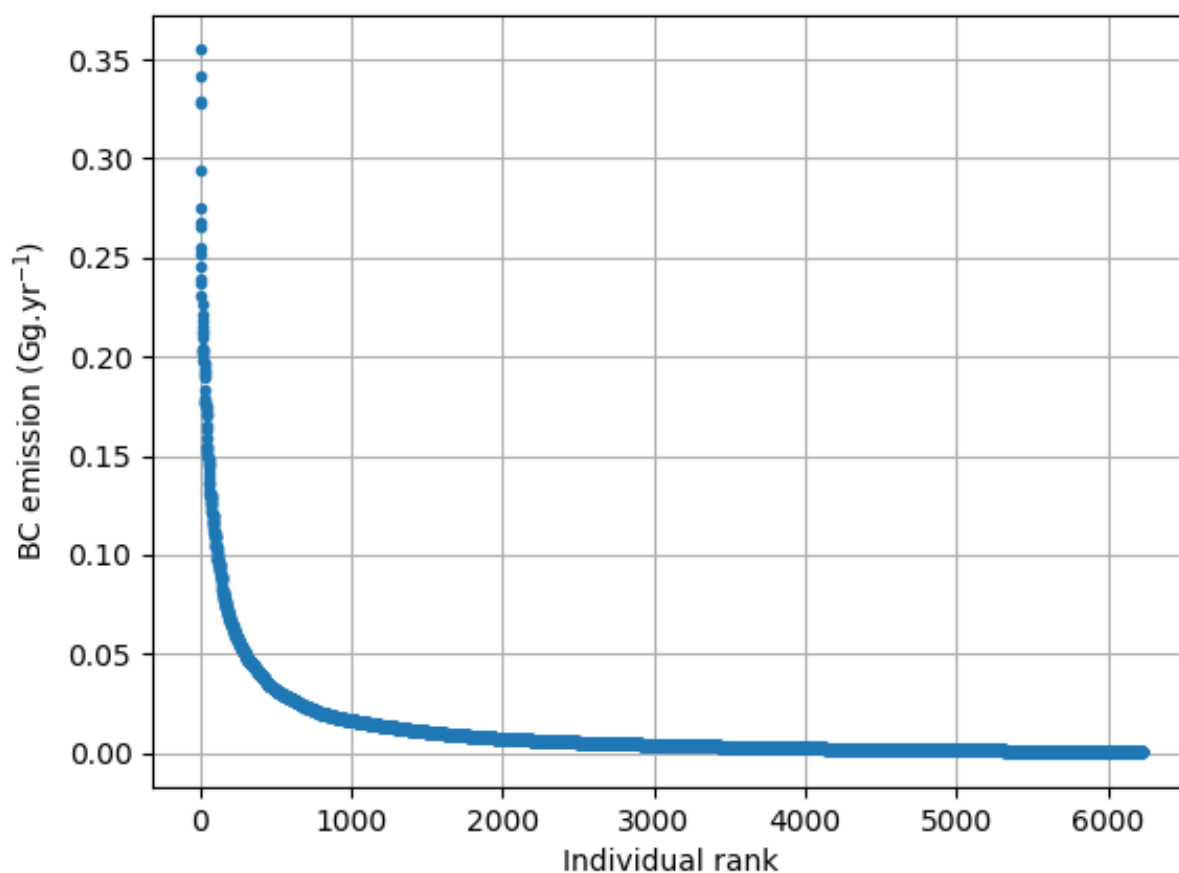
Figure 21. Flaring BC emissions (best estimate, Gg per year) for each individual flaring location (6232 in total).

atmosphere by gas flaring in 2017 is 73.4 Gg. With Iraq, Iran, Russia and Algeria being responsible for roughly one half of those emissions. The most active flaring location, which is also the one with the highest emissions, is estimated to have yearly emission of 0.35 Gg of BC in 2017.

The flaring activity and the related black carbon emissions product are available with $0.025° \times 0.025°$ resolution on the Emissions of atmospheric Compounds and Compilation of Ancillary Data (ECCAD) web site (https://eccad3.sedoo.fr) for use in, e.g., atmospheric composition modelling studies.
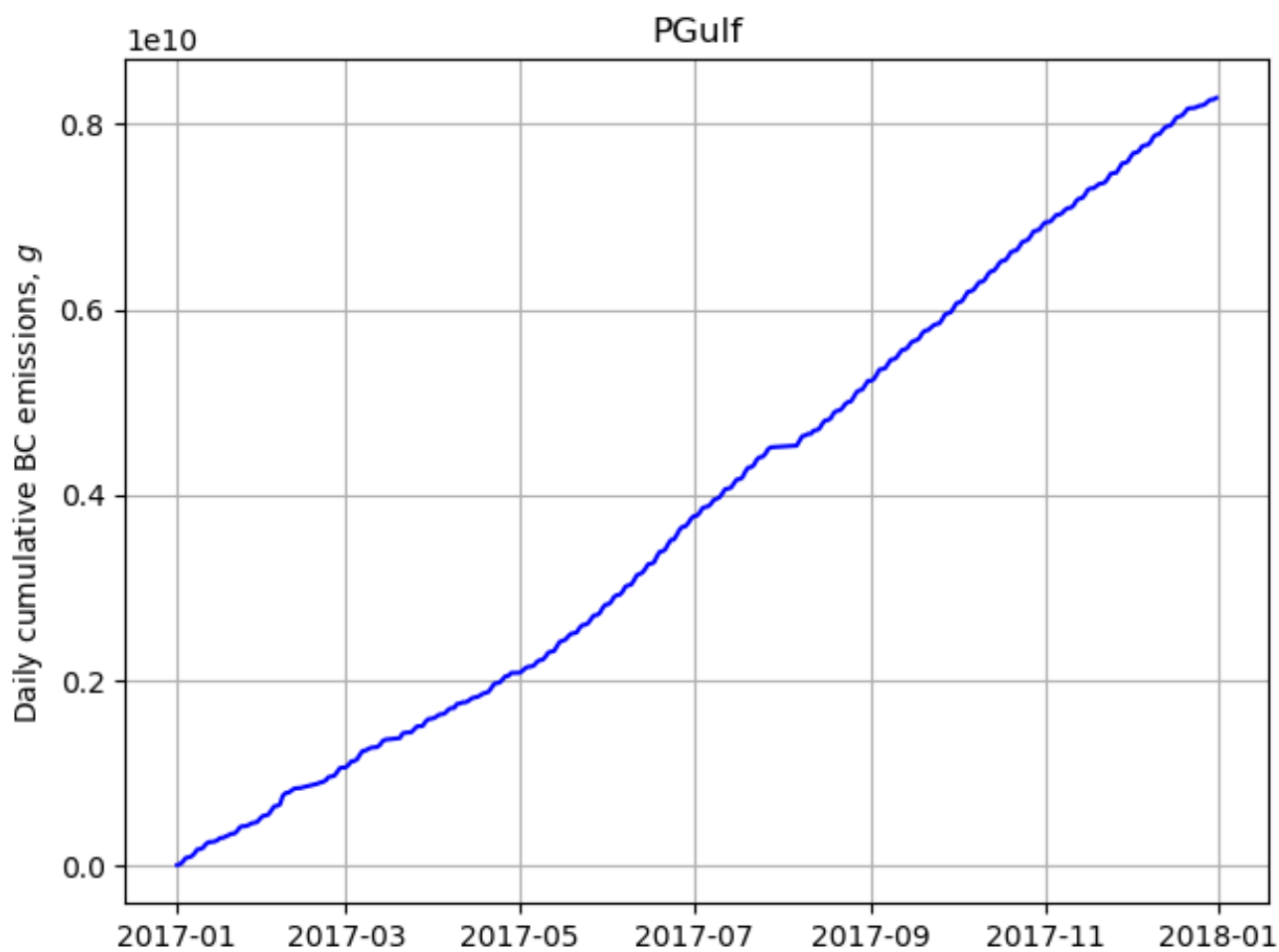
Figure 22. Cumulative total observed BC emissions (BC_{min}, g) in the oil and gas producing region of the Persian gulf, as shown in Figure 10 (1184 flaring locations in the region, aggregated from 41600 high accuracy detections over 348 days).

SLSTR 2017
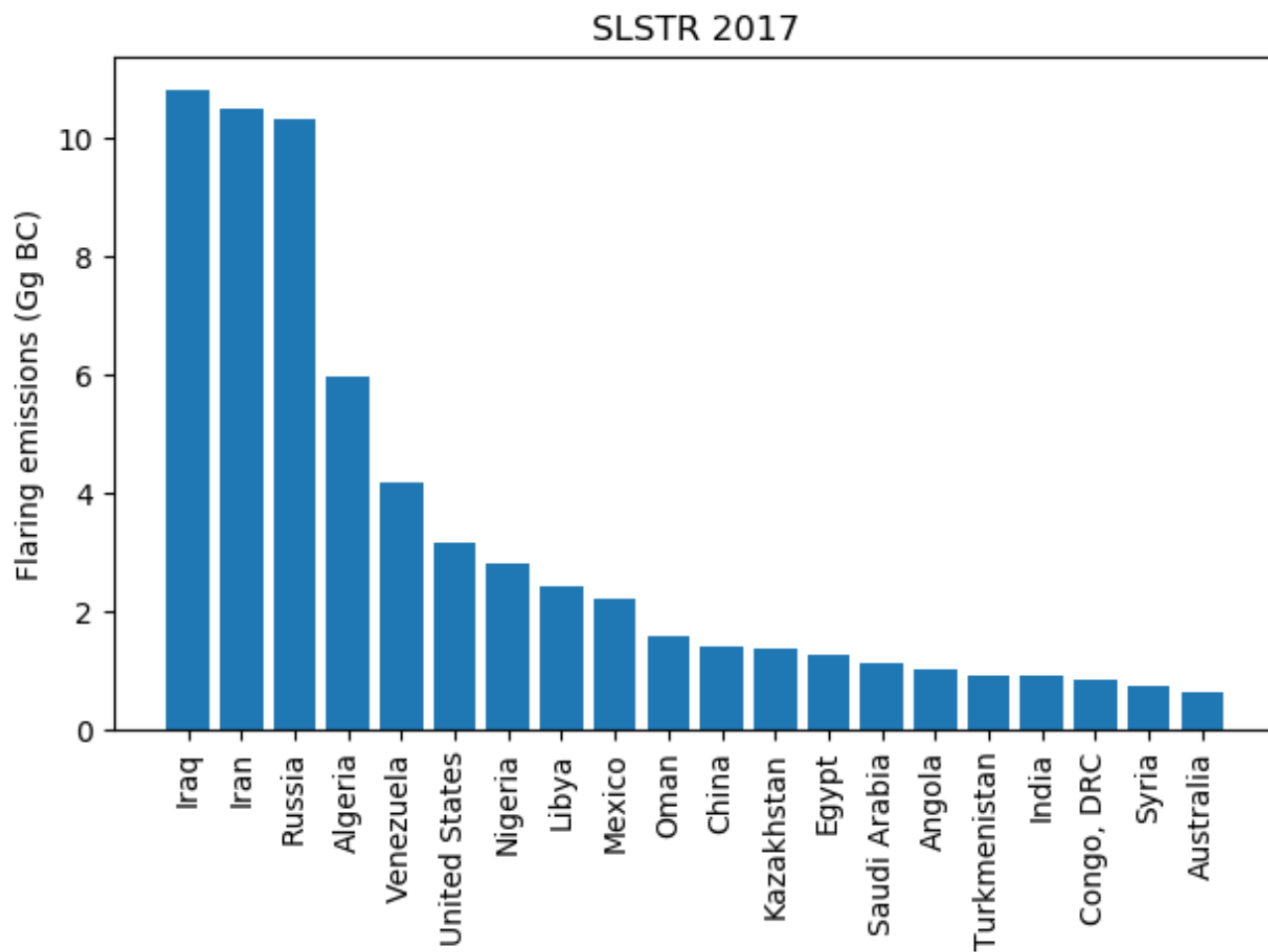
Figure 23. Flaring BC emissions (best estimate, Gg per year) by country, top 20.

5   Data availability

The dataset produced by the described methodology and analysed in this paper is available at https://eccad3.sedoo.fr/#GFlaringS3 with the DOI 10.25326/19 (Caseiro and Kaiser, 2019).

Author contributions. Conceptualization, AC and JWK; Methodology, AC and JWK; Software, AC and DL; Validation, AC, JWK and BG; Formal Analysis, Investigation & Resources, AC and BG; Data Curation, AC, BG and JWK; Writing–Original Draft Preparation, AC; Writing—Review & Editing, BG, JWK & GR; Visualization, AC; Supervision, Project Administration & Funding Acquisition, JWK and GR.

5 *Competing interests.* The authors declare that there are no competing interests.

Acknowledgements. The data was produced in the project "GFS3 - Identification of gas flares and quantification of their emissions using Sentinel-3 SLSTR" funded by the German Federal Ministry for Economic Affairs and Energy (BMWi, Bundesministerium für Wirtschaft und Energie) under contract number FKZ 50EE1339.

References

Ahmed Osama Abdulrahman, Donald Huisingh, and Wim Hafkamp: Sustainability improvements in Egypt's oil & gas industry by implementation of flare gas recovery, Journal of Cleaner Production, 98, 116 – 122, https://doi.org/https://doi.org/10.1016/j.jclepro.2014.11.086, http://www.sciencedirect.com/science/article/pii/S0959652614013894, special Volume: Support your future today! Turn environmental challenges into opportunities., 2015.

Ajao, E. A. and Anurigwo, S.: Land-Based Sources of Pollution in the Niger Delta, Nigeria, Ambio, 13, 442–445, 2002.

Akinola, A. O.: Resource Misgovernance and the Contradictions of Gas Flaring in Nigeria: A Theoretical Conversation, Journal of Asian and African Studies, 53, 749–763, https://doi.org/10.1177/0021909617722374, https://doi.org/10.1177/0021909617722374, 2018.

Anejionu, O. C., Blackburn, G. A., and Whyatt, J. D.: Detecting gas flares and estimating flaring volumes at individual flow stations using {MODIS} data, Remote Sensing of Environment, 158, 81 – 94, https://doi.org/http://dx.doi.org/10.1016/j.rse.2014.11.018, http://www.sciencedirect.com/science/article/pii/S003442571400460X, 2015.

Anejionu, O. C. D., Blackburn, G. A., and Whyatt, J. D.: Satellite survey of gas flares: development and application of a Landsat-based technique in the Niger Delta, International Journal of Remote Sensing, 35, 1900–1925, https://doi.org/10.1080/01431161.2013.879351, http://dx.doi.org/10.1080/01431161.2013.879351, 2014.

Anomohanran, O.: Determination of greenhouse gas emission resulting from gas flaring activities in Nigeria, Energy Policy, 45, 666 – 670, https://doi.org/http://dx.doi.org/10.1016/j.enpol.2012.03.018, http://www.sciencedirect.com/science/article/pii/S0301421512002236, 2012.

Bond, T. C., Doherty, S. J., Fahey, D. W., Forster, P. M., Berntsen, T., DeAngelo, B. J., Flanner, M. G., Ghan, S., K§rcher, B., Koch, D., Kinne, S., Kondo, Y., Quinn, P. K., Sarofim, M. C., Schultz, M. G., Schulz, M., Venkataraman, C., Zhang, H., Zhang, S., Bellouin, N., Guttikunda, S. K., Hopke, P. K., Jacobson, M. Z., Kaiser, J. W., Klimont, Z., Lohmann, U., Schwarz, J. P., Shindell, D., Storelvmo, T., Warren, S. G., and Zender, C. S.: Bounding the role of black carbon in the climate system: A scientific assessment, Journal of Geophysical Research: Atmospheres, 118, 5380–5552, https://doi.org/10.1002/jgrd.50171, http://dx.doi.org/10.1002/jgrd.50171, 2013.

Casadio, S., Arino, O., and Minchella, A.: Use of {ATSR} and {SAR} measurements for the monitoring and characterisation of night-time gas flaring from off-shore platforms: The North Sea test case, Remote Sensing of Environment, 123, 175 – 186, https://doi.org/http://dx.doi.org/10.1016/j.rse.2012.03.021, http://www.sciencedirect.com/science/article/pii/S003442571200140X, 2012a.

Casadio, S., Arino, O., and Serpe, D.: Gas flaring monitoring from space using the {ATSR} instrument series, Remote Sensing of Environment, 116, 239 – 249, https://doi.org/http://dx.doi.org/10.1016/j.rse.2010.11.022, http://www.sciencedirect.com/science/article/pii/S0034425711002240, advanced Along Track Scanning Radiometer(AATSR) Special Issue, 2012b.

Caseiro, A. and Kaiser, J. W.: Global Gas Flaring activity and Black Carbon emissions, data, https://doi.org/10.25326/19, https://permalink.aeris-data.fr/GFlaringS3, 2019.

Caseiro, A., Rücker, G., Tiemann, J., Leimbach, D., Lorenz, E., Frauenberger, O., and Kaiser, J. W.: Persistent Hot Spot Detection and Characterisation Using SLSTR, Remote Sensing, 10, https://doi.org/10.3390/rs10071118, http://www.mdpi.com/2072-4292/10/7/1118, 2018.

Chowdhury, S., Shipman, T., Chao, D., Elvidge, C., Zhizhin, M., and Hsu, F.: Daytime gas flare detection using Landsat-8 multispectral data, in: 2014 IEEE Geoscience and Remote Sensing Symposium, pp. 258–261, https://doi.org/10.1109/IGARSS.2014.6946406, 2014.

Doherty, S. J., Warren, S. G., Grenfell, T. C., Clarke, A. D., and Brandt, R. E.: Light-absorbing impurities in Arctic snow, Atmospheric Chemistry and Physics, 10, 11 647–11 680, https://doi.org/10.5194/acp-10-11647-2010, https://www.atmos-chem-phys.net/10/11647/2010/, 2010.

Doumbia, E. H. T., Liousse, C., Keita, S., Granier, L., Granier, C., Elvidge, C. D., Elguindi, N., and Law, K.: Flaring emissions in Africa: Distribution, evolution and comparison with current inventories, Atmospheric Environment, 199, 423 – 434, https://doi.org/https://doi.org/10.1016/j.atmosenv.2018.11.006, http://www.sciencedirect.com/science/article/pii/S1352231018307726, 2019.

Elvidge, C. D., Imhoff, M. L., Baugh, K. E., Hobson, V. R., Nelson, I., Safran, J., Dietz, J. B., and Tuttle, B. T.: Night-time lights of the world: 1994‚Äì1995, {ISPRS} Journal of Photogrammetry and Remote Sensing, 56, 81 – 99, https://doi.org/http://dx.doi.org/10.1016/S0924-2716(01)00040-5, http://www.sciencedirect.com/science/article/pii/S0924271601000405, 2001.

Elvidge, C. D., Baugh, K. E., Tuttle, B. T., Howard, A. T., Pack, D. W., Milesi, C., and Erwin, E. H.: A Twelve Year Record of National and Global Gas Flaring Volumes Estimated Using Satellite Data, Tech. rep., World Bank, 2007.

Elvidge, C. D., Baugh, K., Tuttle, B., Ziskin, D., Ghosh, T., Zhizhin, M., and Pack, D.: Improving Satellite Data Estimation of Gas Flaring Volumes, Tech. rep., GGFR - World Bank, 2009.

Elvidge, C. D., Zhizhin, M., Hsu, F.-C., and Baugh, K. E.: VIIRS Nightfire: Satellite Pyrometry at Night, Remote Sensing, 5, 4423–4449, https://doi.org/10.3390/rs5094423, http://www.mdpi.com/2072-4292/5/9/4423, 2013.

Elvidge, C. D., Zhizhin, M., Baugh, K., Hsu, F.-C., and Ghosh, T.: Methods for Global Survey of Natural Gas Flaring from Visible Infrared Imaging Radiometer Suite Data, Energies, 9, 14, https://doi.org/10.3390/en9010014, http://www.mdpi.com/1996-1073/9/1/14, 2016.

Elvidge, C. D., Bazilian, M. D., Zhizhin, M., Ghosh, T., Baugh, K., and Hsu, F.-C.: The potential role of natural gas flaring in meeting greenhouse gas mitigation targets, Energy Strategy Reviews, 20, 156 – 162, https://doi.org/https://doi.org/10.1016/j.esr.2017.12.012, http://www.sciencedirect.com/science/article/pii/S2211467X17300962, 2018.

Emeka Ojijiagwo, Chike F. Oduoza, and Nwabueze Emekwuru: Economics of gas to wire technology applied in gas flare management, Engineering Science and Technology, an International Journal, 19, 2109 – 2118, https://doi.org/https://doi.org/10.1016/j.jestch.2016.09.012, http://www.sciencedirect.com/science/article/pii/S2215098616307765, 2016.

Evangeliou, N., Shevchenko, V. P., Yttri, K. E., Eckhardt, S., Sollum, E., Pokrovsky, O. S., Kobelev, V. O., Korobov, V. B., Lobanov, A. A., Starodymova, D. P., Vorobiev, S. N., Thompson, R. L., and Stohl, A.: Origin of elemental carbon in snow from western Siberia and northwestern European Russia during winter–spring 2014, 2015 and 2016, Atmospheric Chemistry and Physics, 18, 963–977, https://doi.org/10.5194/acp-18-963-2018, https://www.atmos-chem-phys.net/18/963/2018/, 2018.

Faruolo, M., Coviello, I., Filizzola, C., Lacava, T., Pergola, N., and Tramutoli, V.: A satellite-based analysis of the Val d'Agri Oil Center (southern Italy) gas flaring emissions, Natural Hazards and Earth System Science, 14, 2783–2793, https://doi.org/10.5194/nhess-14-2783-2014, http://www.nat-hazards-earth-syst-sci.net/14/2783/2014/, 2014.

Faruolo, M., Lacava, T., Pergola, N., and Tramutoli, V.: On the Potential of the RST-FLARE Algorithm for Gas Flaring Characterization from Space, Sensors, 18, https://doi.org/10.3390/s18082466, http://www.mdpi.com/1424-8220/18/8/2466, 2018.

Flanner, M. G., Zender, C. S., Randerson, J. T., and Rasch, P. J.: Present-day climate forcing and response from black carbon in snow, Journal of Geophysical Research: Atmospheres, 112, https://doi.org/10.1029/2006JD008003, https://agupubs.onlinelibrary.wiley.com/doi/abs/10.1029/2006JD008003, 2007.

Franklin, M., Chau, K., Cushing, L. J., and Johnston, J. E.: Characterizing Flaring from Unconventional Oil and Gas Operations in South Texas Using Satellite Observations, Environmental Science & Technology, 0, null, https://doi.org/10.1021/acs.est.8b05355, https://doi.org/10.1021/acs.est.8b05355, pMID: 30657671, 2019.

Gabriele Comodi, Massimiliano Renzi, and Mosè Rossi: Energy efficiency improvement in oil refineries through flare gas recovery technique to meet the emission trading targets, Energy, 109, 1 – 12, https://doi.org/https://doi.org/10.1016/j.energy.2016.04.080, http://www.sciencedirect.com/science/article/pii/S0360544216304935, 2016.

Hansen, J. and Nazarenko, L.: Soot climate forcing via snow and ice albedos, Proceedings of the National Academy of Sciences, 101, 423–428, https://doi.org/10.1073/pnas.2237157100, http://www.pnas.org/cgi/doi/10.1073/pnas.2237157100, 2004.

Heinrich, U., Dungworth, D. L., Pott, F., Peters, L., Dasenbrock, C., Levsen, K., Koch, W., Creutzenberg, O., and Schulte, A.: The Carcinogenic Effects of Carbon Black Particles and Tar‚ÄìPitch Condensation Aerosol after Inhalation Exposure of Rats, Annals of Occupational Hygiene, 38, 351–356, https://doi.org/10.1093/annhyg/38.inhaled_particles_VII.351, http://annhyg.oxfordjournals.org/content/38/inhaled_particles_VII/351.abstract, 1994.

Huang, K. and Fu, J. S.: A global gas flaring black carbon emission rate dataset from 1994 to 2012, Scientific Data, 3, https://doi.org/10.1038/sdata.2016.104, http://dx.doi.org/10.1038/sdata.2016.104, 2016.

Huang, K., Fu, J. S., Prikhodko, V. Y., Storey, J. M., Romanov, A., Hodson, E. L., Cresko, J., Morozova, I., Ignatieva, Y., and Cabaniss, J.: Russian anthropogenic black carbon: Emission reconstruction and Arctic black carbon simulation, Journal of Geophysical Research: Atmospheres, 120, 11,306–11,333, https://doi.org/10.1002/2015JD023358, http://dx.doi.org/10.1002/2015JD023358, 2015JD023358, 2015.

IPCC: Climate Change 2013: The Physical Science Basis. Contribution of Working Group I to the Fifth Assessment Report of the Intergovernmental Panel on Climate Change, Cambridge University Press, Cambridge, United Kingdom and New York, NY, USA, https://doi.org/10.1017/CBO9781107415324, www.climatechange2013.org, 2013.

Ismail, O. and Umukoro, G.: Global Impact of Gas Flaring, Energy and Power Engineering, 4, 290 – 302, https://doi.org/10.4236/epe.2012.44039, http://www.scirp.org/journal/PaperInformation.aspx?PaperID=20231#.VZvUq8789Ro, 2012.

Julius, O. O.: Environmental impact of gas flaring within Umutu-Ebedei gas plant in Delta State, Nigeria, Archives of Applied Science Research, 3, 272–279, 2011.

Klimont, Z., Kupiainen, K., Heyes, C., Purohit, P., Cofala, J., Rafaj, P., Borken Kleefeld, J., and Schöpp, W.: Global anthropogenic emissions of particulate matter including black carbon, Atmospheric Chemistry and Physics, 17, 8681–8723, https://doi.org/10.5194/acp-17-8681-2017, https://www.atmos-chem-phys.net/17/8681/2017/, 2017.

Li, C., Hsu, N. C., Sayer, A. M., Krotkov, N. A., Fu, J. S., Lamsal, L. N., Lee, J., and Tsay, S.-C.: Satellite observation of pollutant emissions from gas flaring activities near the Arctic, Atmospheric Environment, 133, 1 – 11, https://doi.org/http://dx.doi.org/10.1016/j.atmosenv.2016.03.019, http://www.sciencedirect.com/science/article/pii/S1352231016301893, 2016.

Liu, Y., Hu, C., Zhan, W., Sun, C., Murch, B., and Ma, L.: Identifying industrial heat sources using time-series of the VIIRS Nightfire product with an object-oriented approach, Remote Sensing of Environment, 204, 347 – 365, https://doi.org/https://doi.org/10.1016/j.rse.2017.10.019, http://www.sciencedirect.com/science/article/pii/S0034425717304820, 2018.

McEwen, J. D. and Johnson, M. R.: Black carbon particulate matter emission factors for buoyancy-driven associated gas flares, Journal of the Air & Waste Management Association, 62, 307–321, https://doi.org/10.1080/10473289.2011.650040, http://dx.doi.org/10.1080/10473289.2011.650040, 2012.

Nwaichi, E. and Uzazobona, M.: Estimation of the CO_2 Level due to Gas Flaring in the Niger Delta, Research Journal of Environmental Sciences, 5, 565–572, https://doi.org/10.3923/rjes.2011.565.572, http://scialert.net/abstract/?doi=rjes.2011.565.572, 2011.

Nwoye, C. I., Nwakpa, S. O., Nwosu, I. E., Odo, J. U., Chinwuko, E. C., and Idenyi, N. E.: Multi-Factorial Analysis of Atmospheric Noise Pollution Level Based on Emitted Carbon and Heat Radiation during Gas Flaring, Journal of Atmospheric Pollution, 2, 22–29, https://doi.org/10.12691/jap-2-1-5, http://pubs.sciepub.com/jap/2/1/5, 2014.

Obioh, I., Oluwole, A. F., and Akeredolu, F. A.: Non-CO_2 gaseous emissions from upstream oil and gas operations in Nigeria, Environmental Monitoring and Assessment, 31, 67–72, 1994.

Olivier, J., Janssens Maenhout, G., Muntean, M., and Peters, J.: Trends in global CO2 emissions: 2014 Report, Tech. rep., European Commission, Joint Research Centre (JRC), Institute for Environment and Sustainability (IES), PBL Netherlands Environmental Assessment Agency, The Hague, 2014.

Onu, P. u., Quan, X., and Ling, X.: Acid rain: an analysis on the cause, impacts and abatement measures Niger Delta perspective, Nigeria., International Journal of Scientific & Engineering Research, 5, 1214–1219, 2014.

Papailias, G. and Mavroidis, I.: Atmospheric Emissions from Oil and Gas Extraction and Production in Greece, Atmosphere, 9, https://doi.org/10.3390/atmos9040152, http://www.mdpi.com/2073-4433/9/4/152, 2018.

Quinn, P. K., Shaw, G., Andrews, E., Dutton, E. G., Ruoho Airola, T., and Gong, S. L.: Arctic haze: current trends and knowledge gaps, Tellus B, 59, 99–114, https://doi.org/10.1111/j.1600-0889.2006.00238.x, http://dx.doi.org/10.1111/j.1600-0889.2006.00238.x, 2007.

Rahimpour, M. R. and Jokar, S. M.: Feasibility of flare gas reformation to practical energy in Farashband gas refinery: No gas flaring, Journal of Hazardous Materials, 209,Äì210, 204 – 217, https://doi.org/http://dx.doi.org/10.1016/j.jhazmat.2012.01.017, http://www.sciencedirect.com/science/article/pii/S0304389412000337, 2012.

Schwarz, J. P., Holloway, J. S., Katich, J. M., McKeen, S., Kort, E. A., Smith, M. L., Ryerson, T. B., Sweeney, C., and Peischl, J.: Black Carbon Emissions from the Bakken Oil and Gas Development Region, Environmental Science & Technology Letters, 2, 281–285, https://doi.org/10.1021/acs.estlett.5b00225, https://doi.org/10.1021/acs.estlett.5b00225, 2015.

Serreze, M. C. and Barry, R. G.: Processes and impacts of Arctic amplification: A research synthesis, Global and Planetary Change, 77, 85 – 96, https://doi.org/https://doi.org/10.1016/j.gloplacha.2011.03.004, http://www.sciencedirect.com/science/article/pii/S0921818111000397, 2011.

Siebert, L., Simkin, T., and Kimberly, P.: Volcanoes of the World: Third Edition, University of California Press, 3 edn., http://www.jstor.org/stable/10.1525/j.ctt1pnqdx, 2010.

Stohl, A., Klimont, Z., Eckhardt, S., Kupiainen, K., Shevchenko, V. P., Kopeikin, V. M., and Novigatsky, A. N.: Black carbon in the Arctic: the underestimated role of gas flaring and residential combustion emissions, Atmospheric Chemistry and Physics, 13, 8833–8855, https://doi.org/10.5194/acp-13-8833-2013, http://www.atmos-chem-phys.net/13/8833/2013/, 2013.

Uzomah, V. and Sangodoyin, A.: Rainwater chemistry as influenced by atmospheric deposition of pollutants in Southern Nigeria, Environmental Management and Health, 11, 149–156, https://doi.org/10.1108/09566160010321569, https://doi.org/10.1108/09566160010321569, 2000.

Venzke, E.: Global Volcanism Program – Volcanoes of the World, v. 4.7.4. Smithsonian Institution. Downloaded 02 Oct 2018, https://doi.org/10.5479/si.GVP.VOTW4-2013, 2013.

Weyant, C. L., Shepson, P. B., Subramanian, R., Cambaliza, M. O. L., Heimburger, A., McCabe, D., Baum, E., Stirm, B. H., and Bond, T. C.: Black Carbon Emissions from Associated Natural Gas Flaring, Environmental Science & Technology, 50, 2075–2081, https://doi.org/10.1021/acs.est.5b04712, http://dx.doi.org/10.1021/acs.est.5b04712, pMID: 26764563, 2016.

Zolfaghari, M., Pirouzfar, V., and Sakhaeinia, H.: Technical characterization and economic evaluation of recovery of flare gas in various gas-processing plants, Energy, 124, 481 – 491, https://doi.org/https://doi.org/10.1016/j.energy.2017.02.084, http://www.sciencedirect.com/science/article/pii/S036054421730258X, 2017.